Frontiers in Heat
and Mass Transfer

Tech Science Press

https://doi.org/10.32604/fhmt.2026.082228

ARTICLE

Numerical Study of Hydrogen Crossover Evolution Inside the Proton Exchange Membrane Fuel Cell under Dynamic Load

Wenxin Luo[1], **Kaiwen Wang**[1], **Pugalenthiyar Thondaiman**[2] and **Qianqian Wang**[1,*]

[1]School of Energy and Power Engineering, University of Shanghai for Science and Technology, Shanghai, China
[2]Department of Advanced Components and Materials Engineering, Sunchon National University, 255, Jungang-ro, Suncheon-si, Jellanamdo, Republic of Korea

*Corresponding Author: Qianqian Wang. Email: qianqianwang@usst.edu.cn

Received: 12 March 2026; Accepted: 23 April 2026; Published: 29 June 2026

ABSTRACT: Hydrogen (H_2) crossover in proton exchange membrane fuel cells (PEMFCs) reduces performance and poses safety risks, but its behavior under rapidly changing loads, which are common in vehicles, is not well understood. To address this, we developed a three-dimensional, two-phase, non-isothermal model that tracks H_2 from dissolution in the anode, through transport across the membrane, to reaction at the cathode. The analysis shows that diffusion dominates whereas convection contributes little. Key findings are as follows: H_2 crossover reduces the open-circuit voltage by 210 mV and raises cathode temperature by approximately 0.2°C; reducing the membrane thickness from 20 to 5 μm increases the crossover current density fourfold (from 2.8–3.6 to 11.4–13.2 mA cm^{-2}); under rapid load changes, transient undershoots of 0.8–1.72 mA cm^{-2} occur because the H_2 concentration drops quickly whereas water and thermal conditions adjust slowly; and a variation of approximately 1 mA cm^{-2} along the flow channel indicates that local H_2 distribution and membrane hydration strongly affect transport. Overall, H_2 crossover under dynamic loads is governed by diffusion as modified by local water and heat distribution, with significant differences between channel and rib regions. These results help predict and mitigate fuel cell degradation in practical applications.

KEYWORDS: Proton exchange membrane fuel cells; hydrogen crossover; numerical simulation; three-dimensional model; dynamic load

1 Introduction

Proton exchange membrane fuel cells (PEMFCs) are considered to be promising power sources for vehicles due to their high efficiency, zero-emission, and quiet operation [1,2]. However, unlike steady-state laboratory testing, automotive applications subject PEMFCs to severe dynamic operating conditions—including rapid load transients during acceleration/deceleration and frequent start-stop cycles—that result in dramatic changes in local water, thermal and chemical conditions [3], fundamentally altering H_2 transport phenomena [4]. Under these dynamic conditions, the undesired hydrogen (H_2) crossover exhibits transient behaviors significantly distinct from steady-state diffusion, yet its spatiotemporal evolution remains poorly understood despite causing membrane thinning and degradation [5–7]. When H_2 crossover occurs, hydrogen is transported to the cathode electrode, where it undergoes reactions generating heat and water, but without contributing to electrical output. Furthermore, hydrogen peroxide radicals can form at potentials below 0.628 V [8]. The elevated local temperature and the presence of hydrogen peroxide radicals can initiate thermal and chemical degradation of the perfluorosulfonic acid (PFSA) ionomer, potentially leading to membrane deterioration, pinhole development [9] and associated safety risks such as hydrogen explosions [5,10,11] over long-term operation. While these long-term degradation mechanisms and safety hazards are not explicitly modeled in the present work, understanding the transient H_2 crossover dynamics and local thermal responses addressed herein provides an essential basis for predicting these phenomena. Therefore, it is crucial to evaluate local H_2 crossover inside PEMFCs, especially in dynamic operating scenarios, considering both efficiency and safety.

Despite extensive research on H_2 crossover, significant knowledge gaps persist regarding its behavior under realistic dynamic operating conditions. Current understanding relies heavily on steady-state investigations, creating a critical disconnect with automotive applications characterized by rapid load transients. Experimental studies have employed both direct and indirect methodologies to quantify H_2 crossover [12]. Direct techniques such as gas chromatography [13], mass spectrometry [10], and volumetric methods [14] provide accurate permeation data, while indirect electrochemical methods including linear sweep voltammetry (LSV) [15], cyclic voltammetry (CV) [16], potential step method (PSM) [17], and galvanostatic charging method (GCM) [18,19] offer operational convenience. However, most electrochemical techniques integrate crossover over the entire membrane area, obscuring local spatial distributions. Although specialized segmented plates [20] and multi-port bipolar plates [21] have enabled localized measurements, such studies remain limited to steady-state conditions with nitrogen-purged cathodes to eliminate reaction interference. Consequently, the online monitoring of local H_2 crossover during actual fuel cell discharge under dynamic loads remains technically unachievable due to intricate mass transfer and reaction complexities.

Theoretical modeling offers an alternative to resolve spatial and temporal distributions, providing equipment-independent, cost-effective, and accessible benefits [4,22–25], yet current approaches exhibit systematic simplifications. Most existing models treat H_2 crossover as steady-state Fickian diffusion through the membrane [26–29], neglecting the complete physicochemical process encompassing gas dissolution, pressure-driven convection, interfacial release, and electrochemical oxidation at the cathode [14,30,31]. While some studies acknowledge pressure-driven convection [32,33] and cathode reaction kinetics [23], few models integrate these mechanisms within a comprehensive multi-physics framework. More critically, the transition from steady-state to dynamic operation has received limited attention [8,34], despite H_2 permeation fluctuations under transient conditions directly governing localized degradation rates. These collective limitations reveal a fundamental research gap: the absence of comprehensive three-dimensional transient models capable of resolving local H_2 crossover dynamics and their coupling with thermal and electrochemical responses under realistic automotive operating scenarios.

To contextualize these limitations and clarify the distinct contributions of the present work, Table 1 systematically compares the key modeling features (dimensionality, thermal coupling, transient capability, and H_2 crossover physics) of the most relevant prior studies [23,27,28] against the proposed framework.

Table 1: Model parameters.

Feature	**Vilekar and Datta [23]**	**Nguyen and Fushinobu [28]**	**Ji et al. [27]**	**Present Work**
Dimensionality	1D/Simplified	2D	2D/Lumped-parameter	3D full-field
Two-phase	No	Yes	Yes	Yes
Thermal coupling	Isothermal (implicit)	Not considered	Simplified/Isothermal	Non-isothermal (full energy equation)
H_2 crossover physics	Steady-state diffusion only	Steady gas permeation	Fick's law coupling	Dissolution-diffusion-convection-reaction

(Continued)

Table 1 (continued)

Feature	Vilekar and Datta [23]	Nguyen and Fushinobu [28]	Ji et al. [27]	Present Work
Transient capability	Steady-state	Steady-state	Quasi-steady	Fully transient
Dynamic load support	Not supported	Not supported	Not supported	Step/ramp load transients

Note: Vilekar and Datta [23] is a baseline steady-state dissolution-diffusion model; Nguyen and Fushinobu [28] represents 2D two-phase steady-state gas crossover; Ji et al. [27] employs Fick's law coupling but lacks full transient thermal-mass coupling.

The main contributions of this study are summarized as follows:

(1) Development of a coupled multi-physics transient model.

Unlike previous studies simplifying H_2 crossover as steady-state diffusion, we establish a three-dimensional, two-phase, non-isothermal transient model integrating H_2 dissolution, diffusion-convection transport, and electrochemical oxidation, coupled with local mass, charge, and heat transfer.

(2) Experimental validation under transient conditions.

The model is validated against experimental data for both steady-state polarization and dynamic voltage responses (step load changes), addressing the critical gap of transient H_2 crossover measurement that direct experimental techniques cannot easily achieve online.

(3) Discovery of transient undershoot mechanisms and parametric effects.

We reveal the undershoot phenomenon (0.8–1.72 mA cm^{-2}) driven by the competition between concentration drop and membrane hydration lag, and quantify effects of membrane thickness (5–20 μm), stoichiometry (0.9–2.0), and humidity (20%–80% RH).

(4) Revealing spatial-temporal variations and establishing foundation for degradation prediction.

We identify contrasting channel-rib evolution patterns during load transients (channel-rib differences of 0.1–0.7 mA cm^{-2}) and quantify humidity-induced spatial variations (~0.8 mA cm^{-2} increase), establishing a mechanistic foundation for subsequent coupling with chemical degradation models.

The remainder of this paper is organized as follows. Section 2 presents the model assumptions. Section 3 describes the development of the PEMFC model coupled with H_2 crossover, including process features and geometric domain, governing equations, reaction kinetics, and boundary conditions. Section 4 presents model implementation and verification, followed by results and discussion of parametric studies and design implications. Finally, Section 5 summarizes the principal findings, discusses model limitations, and outlines future work.

2 Model Assumption

The model is based on the following reasonable assumptions [16]:

(1) All gases behave as ideal gases.
(2) Product water is initially produced in the gas phase and may undergo phase change during transport through the porous layers, forming liquid water.
(3) The membrane is defect-free, and H_2 crossover flux varies spatially with temperature, membrane water content, and current density.
(4) Permeated H_2 reacts electrochemically with O_2.

3 PEMFC Model Coupled with H_2 Crossover

3.1 Process Features and Geometric Domain

As illustrated in Fig. 1a, the operation of hydrogen-powered fuel cells is characterized by frequent fluctuations in current loading over time. This results in real-time variations in internal heat and mass transfer, as well as fluctuations in electrochemical reaction rates within the cell. At the anode catalyst layer (aCL), hydrogen (H_2) undergoes the hydrogen oxidation reaction (HOR), generating protons and electrons at platinum (Pt) catalyst sites. Protons are transported to the cathode catalyst layer (cCL) through ionomer and proton exchange membrane (PEM) phases, while electrons travel through porous carbon materials and external circuitry to the cathode side, performing electrical work during this process. At the cathode, oxygen (O_2) reacts with protons and electrons to form water, releasing significant heat. The transport of mass, heat, and charge within the fuel cell is depicted in Fig. 1b.

The PEM serves the crucial functions of conducting protons and separating anode fuel from cathode oxidant. However, H_2 crossover is unavoidable due to the porous nature of membranes and tends to increase with PEM aging [16,35]. As shown in Fig. 1c, a fraction of H_2 permeates through the membrane via diffusion and convective transport to reach the cCL [33]. Upon reaching the cathode, permeated H_2 undergoes chemical or electrochemical reactions. Most studies indicate that H_2 is completely consumed by O_2 through electrochemical reactions, primarily due to high cathode electrode potentials [15,23,36,37]. Therefore, as shown in Fig. 1c, H_2 reaching the cathode is dissociated into electrons and protons through HOR, which then combine with O_2 within the cCL to undergo oxygen reduction reaction (ORR), thereby forming a local fuel cell. Although HOR and ORR in this local fuel cell consume hydrogen and oxygen to produce water, they do not generate external electrical work. As a result, enthalpy changes from both half-reactions are released as heat, potentially leading to local hot spot formation [38].

H_2 crossover processes are significantly affected by fuel cell operating conditions; therefore, a three-dimensional (3D) PEMFC model was utilized in this study to investigate local H_2 crossover behavior. The model consists of a single channel with a length of 10 mm, as illustrated in Fig. 1b. The geometric domain encompasses the bipolar plate (BP), gas channel (GC), gas diffusion backing layer (GDB), microporous layer (MPL), catalyst layer (CL), and PEM, where lowercase letters "a" and "c" represent the anode and cathode sides, respectively. The geometric configuration and cross-sectional parameters are consistent with specifications detailed in our previous publications on two-dimensional modeling [39,40]. Additional geometric parameters for this model are listed in Table 2.

3.2 Model Equations

This study investigates the evolution of H_2 crossover in PEMFCs under dynamic loading conditions using a three-dimensional, two-phase, non-isothermal, transient model. The model is based on multi-physics conservation equations governing mixture gas flow, gas species transport, dissolved H_2 transport, liquid water transport, membrane water content, energy, and charge. The two-phase flow, heat, and charge transport components are primarily adapted from the one-dimensional and two-dimensional transient models of multi-physics coupled phenomena in PEMFCs developed by Wang et al. [39,41]. Additionally, dissolved H_2 transport in the electrolyte is modeled based on the steady-state model developed by Vilekar and Datta [23].

The symbols and nomenclature used in Eqs. (1)–(37) are defined in Table 3.

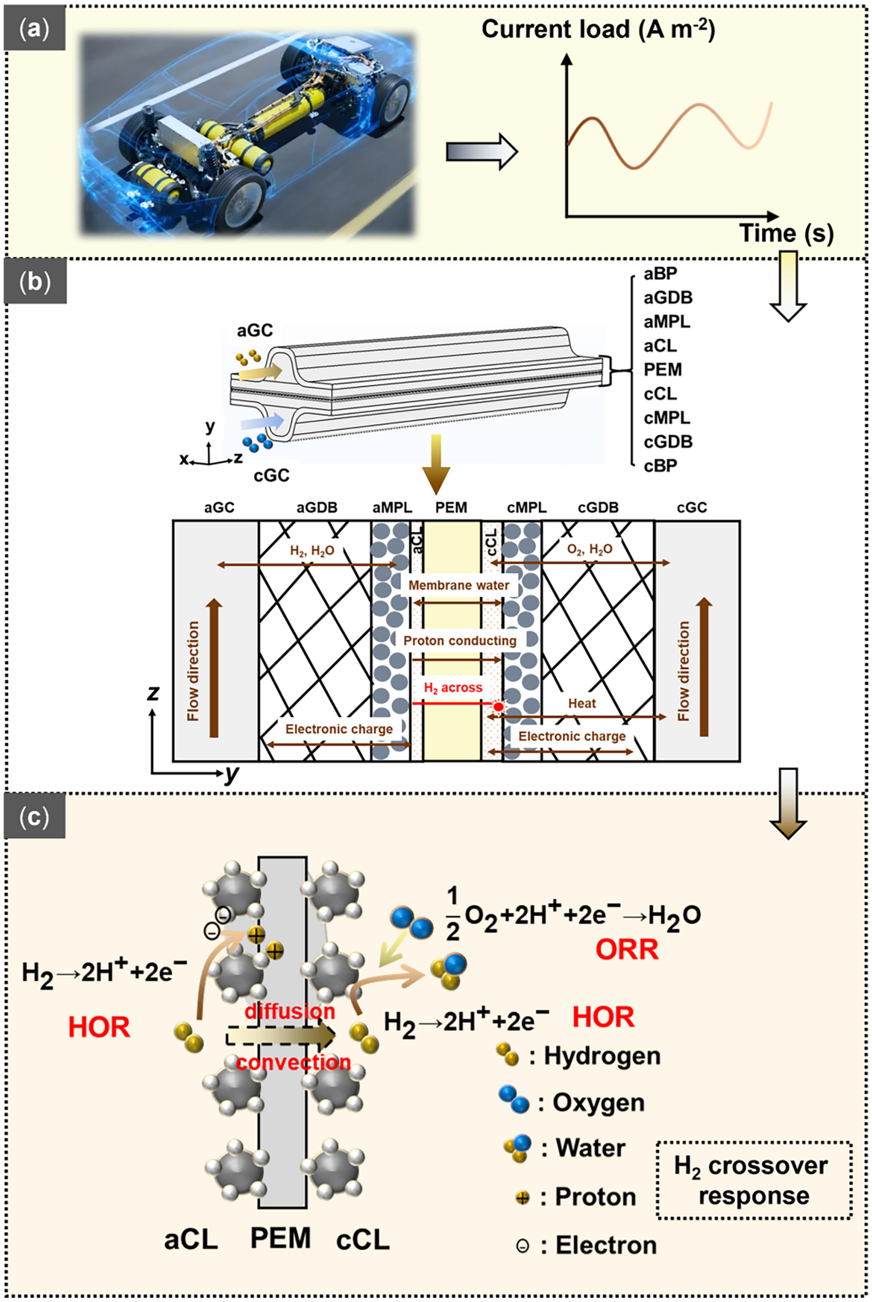

Figure 1: Schematics of (**a**) dynamic load of fuel cell power system, (**b**) single-channel fuel cell 3D geometric model and internal transport process, and (**c**) detailed mechanism of H_2 crossover (dissolution at anode, transport across membrane, and electrochemical reaction at cathode).

Table 2: Model parameters.

Gas Channel Length, Height, Bottom Width, Top Width (mm)	**10, 0.7, 1, 0.5**
Land length, width, thickness (mm)	10, 0.75, 0.1
Thickness of aCLs and cCL (μm)	4, 8
Thickness of MPLs (μm)	30
Thickness of GDBs (μm)	190
Thickness of PEM (μm)	15
Porosity of CLs, MPLs, and GDBs	0.3, 0.6, 0.75
Volume fraction of the Ionomer in CLs	0.3
Hydraulic permeability of liquid water through the membrane (m^2)	1.6×10^{-18}
Mass transport coefficient for gas H_2 to dissolved H_2 (s^{-1})	100,000
Tortuosity of the ionomer	1.5
Membrane water dynamic viscosity (Pa s)	4.7×10^{-4}
Dry membrane density (kg m^{-3})	2000
Enthalpy change for ORR (J mol^{-1})	−241,826
Standard entropy change for ORR (J mol^{-1} K^{-1})	−44.43
Exchange current density for ORR (mA cm^{-2})	1.5×10^{-6}
Exchange current density for HOR (mA cm^{-2})	5
Contact angle of CL, MPL, GDB (°)	100, 130, 140
Surface tension coefficient (N m^{-1})	0.0625
Water evaporation rate (s^{-1})	100
Water condensation rate (s^{-1})	100

Table 3: Nomenclature.

Symbol	Description	Unit
a_{Pt}	Electrocatalytic surface area per unit volume	m^2/m^3
A_{m}	Area of membrane-electrode assembly parallel to flow channel	m^2
A_{ch}	Cross-sectional area of flow channel	m^2
C_{i}	Concentration of gas species i	mol/m^3
$C_{\mathrm{H_2}}$	Hydrogen concentration	mol/m^3
$C_{\mathrm{H_2,diss}}$	Concentration of dissolved H_2	mol/m^3
$C_{\mathrm{H_2,eq}}$	Equilibrium concentration of saturated dissolved H_2	mol/m^3
$C_{\mathrm{H_2}}^{\mathrm{ref}}$	Reference hydrogen concentration	mol/m^3
C_{m}	Concentration of membrane water	mol/m^3
$C_{\mathrm{O_2}}$	Oxygen concentration	mol/m^3
$C_{\mathrm{O_2}}^{\mathrm{ref}}$	Reference oxygen concentration	mol/m^3
$C_{\mathrm{p,g}}$	Specific heat capacity of gas phase	J/(kg K)
$C_{\mathrm{p,i}}$	Specific heat capacity of species i	J/(kg K)
$C_{\mathrm{p,l}}$	Specific heat capacity of liquid water	J/(kg K)
$C_{\mathrm{p,s}}$	Specific heat capacity of solid phase	J/(kg K)
$D_{\mathrm{i}}^{\mathrm{eff}}$	Effective diffusion coefficient of gas species i	m^2/s
$D_{\mathrm{H_2,diss}}$	Effective diffusion coefficient of dissolved H_2 in electrolyte	m^2/s

(Continued)

Table 3 (continued)

Symbol	Description	Unit
$D_{H_2,w}$	Diffusion coefficient of dissolved H_2 in pure water	m^2/s
D_m^{eff}	Effective diffusion coefficient of membrane water	m^2/s
F	Faraday constant	C/mol
f_v	Water volume fraction within ionomer	–
$I(t)$	Time-varying current load	A/m^2
$i_{0,a}^{ref}$	Reference exchange current density for HOR	A/m^2
$i_{0,c}^{ref}$	Reference exchange current density for ORR	A/m^2
J_a	Volumetric current density of HOR at anode	A/m^3
J_c	Volumetric current density of ORR at cathode	A/m^3
J_{cross}	Volumetric current density from HOR of permeated H_2 at cathode	A/m^3
k^{eff}	Effective thermal conductivity	W/(m K)
k_{diss}	Mass transport coefficient for H_2 dissolution	s^{-1}
K_{ml}	Hydraulic permeability of liquid water through membrane	m^2
M_{H_2}	Molar mass of hydrogen	kg/mol
M_{H_2O}	Molar mass of water	kg/mol
M_{O_2}	Molar mass of oxygen	kg/mol
n_d	Electro-osmotic drag coefficient	–
p_{ml}	Membrane water pressure	Pa
$p_{g,a}$	Gas pressure at anode inlet	Pa
$p_{g,c}$	Gas pressure at cathode inlet	Pa
p_{H_2}	Partial pressure of H_2 in pore space	Pa
p_{sat}	Saturation vapor pressure	Pa
R	Universal gas constant	J/(mol K)
RH_a, RH_c	Relative humidity at anode/cathode inlets	–
s	Liquid water saturation	–
S_e	Source term for electrons	A/m^3
S_g	Mass source term for gas mixture	$kg/(m^3\ s)$
S_H	Source term for protons	A/m^3
S_{H_2}	Source term for hydrogen gas	$mol/(m^3\ s)$
$S_{H_2,diss}$	Source term for H_2 dissolution from pores into ionomer	$mol/(m^3\ s)$
S_{H_2O}	Source term for water vapor	$mol/(m^3\ s)$
$S_{H_2,w}$	Solubility of hydrogen in pure water	$mol/(m^3\ Pa)$
S_i	Source term for gas species i	$mol/(m^3\ s)$
S_l	Mass source term for liquid water	$kg/(m^3\ s)$
S_{ml}	Mass source for liquid mixture in membrane	$kg/(m^3\ s)$
S_{O_2}	Source term for oxygen gas	$mol/(m^3\ s)$
$S_{r,diss}$	Mass source for dissolved H_2 consumption by HOR in CCL	$mol/(m^3\ s)$
S_T	Heat source term	W/m^3
S_T^{v-d}	Heat associated with water adsorption	W/m^3
S_T^{v-l}	Heat associated with water condensation	W/m^3
S_{v-d}	Quantity of gaseous water adsorbed by ionomers	$mol/(m^3\ s)$

(Continued)

Table 3 (continued)

Symbol	Description	Unit
$S_{\mathrm{v-l}}$	Amount of gaseous water condensing into liquid water	mol/(m^3 s)
T	Temperature	K
u_{a}	Inlet flow velocity at anode	m/s
u_{c}	Inlet flow velocity at cathode	m/s
$\boldsymbol{u}_{\mathrm{g}}$	Velocity of gas mixture	m/s
$\boldsymbol{u}_{\mathrm{H_2,diss}}$	Convection velocity of liquid mixture (membrane water + dissolved H_2)	m/s
$\boldsymbol{u}_{\mathrm{l}}$	Velocity of liquid water	m/s
ε	Volumetric porosity of porous materials	–
ε_{m}	Ionomer volume fraction	–
η_{a}	Overpotential for HOR at anode	V
η_{c}	Overpotential for ORR at cathode	V
η_{cross}	Overpotential for HOR at cathode	V
ξ_{a}	Stoichiometric ratio of H_2 at anode	–
ξ_{c}	Stoichiometric ratio of O_2 at cathode	–
ρ_{g}	Density of gas mixture	kg/m^3
ρ_{l}	Density of liquid water	kg/m^3
ρ_{s}	Density of solid phase	kg/m^3
$\sigma_{\mathrm{e}}^{\mathrm{eff}}$	Effective electron conductivity	S/m
$\sigma_{\mathrm{m}}^{\mathrm{eff}}$	Effective proton conductivity	S/m
τ	Tortuosity of ionomer	–
ϕ_{e}	Electronic potential	V
$\phi_{\mathrm{eq,a}}$	Equilibrium potential for HOR	V
$\phi_{\mathrm{eq,c}}$	Equilibrium potential for ORR	V
ϕ_{m}	Proton potential	V
ΔH_{hor}	Enthalpy change of HOR	J/mol
ΔH_{orr}	Enthalpy change of ORR	J/mol
μ_{l}	Dynamic viscosity of water	Pa s

3.2.1 H_2 Crossover Transport

The conservation of H_2 in the electrolyte involves three key processes: (1) dissolution of H_2 at the anode from pores into water-saturated ionomer [37], (2) diffusion and convection of molecular H_2 through the membrane from ACL to CCL, driven by concentration and pressure gradients [42], and (3) hydrogen oxidation reaction of dissolved H_2 at the cathode [23], as well as release of dissolved H_2 from the electrolyte into pores within the CCL, as illustrated in Fig. 2.

These processes are mathematically described by the dissolved hydrogen transport equation group (Eqs. (1)–(10)).

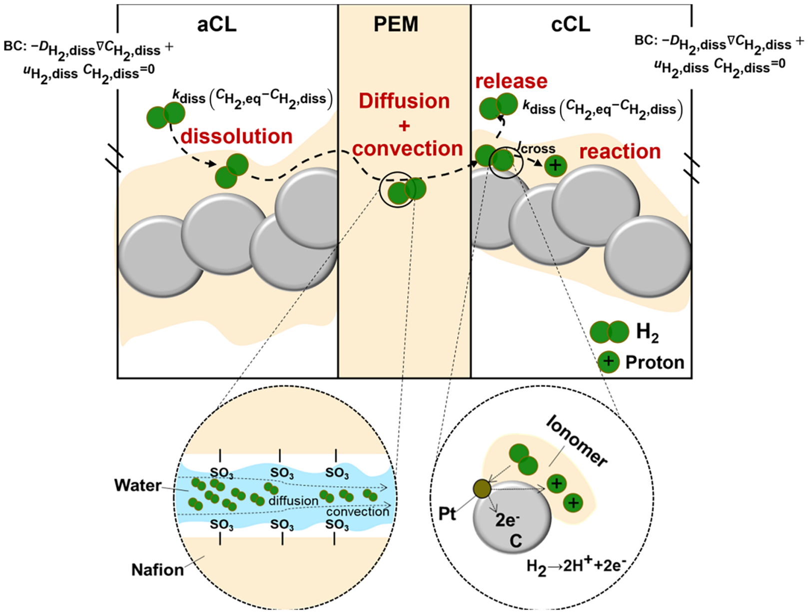

Figure 2: Schematic illustration of H_2 crossover mechanism showing the three key processes: (1) dissolution of H_2 into ionomer at aCL, (2) diffusion and convection through PEM, and (3) electrochemical reaction at cCL, with detailed insets of Nafion microstructure and Pt catalyst reaction.

Dissolved H_2 transport in ionomer phases of the CL and PEM is described by the following mass conservation equation:

$$\frac{\partial C_{H_2,diss}}{\partial t} + \nabla \cdot \left(C_{H_2,diss} \boldsymbol{u}_{H_2,diss} \right) + \nabla \cdot \left(-D_{H_2,diss} \nabla C_{H_2,diss} \right) = S_{H_2,diss} - S_{r,diss} \tag{1}$$

where $C_{H_2,diss}$ is the concentration of dissolved H_2; $\boldsymbol{u}_{H_2,diss}$ denotes the convection velocity of the liquid mixture (membrane water and dissolved H_2) in the membrane; $D_{H_2,diss}$ represents the effective diffusion coefficient of dissolved H_2 in the electrolyte. The effect of membrane water content on H_2 crossover is reflected in the water-dependent diffusion coefficient, which is calculated using the following equation [42–44]:

$$D_{H_2,diss} = \frac{\varepsilon_m f_v}{\tau} D_{H_2,w} \tag{2}$$

where ε_m, f_v and τ represent the ionomer volume fraction, water volume fraction within the ionomer, and tortuosity of the ionomer, respectively. $D_{H_2,w}$ is the diffusion coefficient of dissolved H_2 in pure water, which can be obtained from the following equation [43]:

$$D_{H_2,w} = 4.9e^{-6} \exp\left(\frac{-16{,}560.885}{RT} \right) \tag{3}$$

Convection of the liquid mixture follows Darcy's law and is analyzed using the mass conservation equation for the liquid mixture (Eq. (4)) and Darcy's equation (Eq. (5)), applicable to the CLs and PEM [44,45]. Given the negligible concentration of dissolved H_2, physical properties of the mixed solution, including density and viscosity, are approximated by those of liquid water.

$$\frac{\partial}{\partial t}\left(\varepsilon_{\mathrm{m}} f_{\mathrm{v}} \rho_{\mathrm{l}}\right) + \nabla \cdot \rho_{\mathrm{l}} \boldsymbol{u}_{\mathrm{H_2,diss}} = S_{\mathrm{ml}} \tag{4}$$

$$\boldsymbol{u}_{\mathrm{H_2,diss}} = -f_{\mathrm{v}} \frac{K_{\mathrm{ml}}}{\mu_{\mathrm{l}}} \nabla p_{\mathrm{ml}} \tag{5}$$

where ε_{m} is the volume fraction of ionomer; ρ_{l} is the density of liquid water; K_{ml} is the hydraulic permeability of liquid water through the membrane; μ_{l} is the dynamic viscosity of water; and p_{ml} denotes membrane water pressure.

To quantitatively evaluate the relative contributions of diffusion and convection to hydrogen transport across the membrane, an order-of-magnitude analysis is conducted. The diffusion flux is expressed as $J_{\mathrm{diff}} = -D_{\mathrm{H_2,diss}} \cdot \frac{\Delta C_{\mathrm{H_2,diss}}}{\delta_{\mathrm{mem}}}$, where $\Delta C_{\mathrm{H_2,diss}}$ is the concentration difference across the membrane and δ_{mem} denotes the membrane thickness. The convective flux is estimated by $J_{\mathrm{conv}} = C_{\mathrm{H_2,diss}} \cdot f_{\mathrm{v}} \cdot \frac{K_{\mathrm{ml}}}{\mu_{\mathrm{l}}} \cdot \frac{\Delta p_{\mathrm{ml}}}{\delta_{\mathrm{mem}}}$, with Δp_{ml} representing the pressure difference. Using typical parameter values for a PEMFC—$D_{\mathrm{H_2,diss}} \sim 10^{-10}\ \mathrm{m^2\ s^{-1}}$, $\Delta C_{\mathrm{H_2,diss}} \sim 100\ \mathrm{mol\ m^{-3}}$, $\delta_{\mathrm{mem}} \sim 10^{-5}\mathrm{m}$, $C_{\mathrm{H_2,diss}} \sim 10^{-1}\ \mathrm{mol\ m^{-3}}$, $f_{\mathrm{v}} \sim 10^{-1}$, $K_{\mathrm{ml}} \sim 10^{-19}\ \mathrm{m^2}$, $\mu_{\mathrm{l}} \sim 10^{-4}\ \mathrm{kg\ m^{-1}\ s^{-1}}$, and $\Delta p_{\mathrm{ml}} \sim 10^4$ Pa—the fluxes are estimated to be $J_{\mathrm{diff}} \sim 10^{-5}\ \mathrm{mol\ m^{-2}\ s^{-1}}$ and $J_{\mathrm{conv}} \sim 10^{-8}\ \mathrm{mol\ m^{-2}\ s^{-1}}$. Under the simulated operating conditions, diffusion dominates over convection by approximately three orders of magnitude. Although convection is negligible under the conditions considered, the full convection–diffusion formulation is retained for two main reasons: (i) it enhances the model's generality, enabling its applicability to scenarios with more significant pressure gradients, such as during transient startup/shutdown, variations in membrane compression, or high differential pressure operation and (ii) it facilitates a more comprehensive mechanistic analysis of crossover dynamics without imposing a priori assumptions.

The term $S_{\mathrm{H_2,diss}}$ in Eq. (1) represents the source term for $\mathrm{H_2}$ dissolution from pores into water-saturated ionomer in the CLs, expressed as follows [43]:

$$S_{\mathrm{H_2,diss}} = k_{\mathrm{diss}} \left(C_{\mathrm{H_2,eq}} - C_{\mathrm{H_2,diss}}\right) \tag{6}$$

where k_{diss} represents the mass transport coefficient, and $C_{\mathrm{H_2,eq}}$ denotes the equilibrium concentration of saturated dissolved $\mathrm{H_2}$, as described by Henry's law [43,46].

$$C_{\mathrm{H_2,eq}} = S_{\mathrm{H_2,w}} p_{\mathrm{H_2}} \tag{7}$$

where $p_{\mathrm{H_2}}$ represents the partial pressure of $\mathrm{H_2}$ in the pore space, and $S_{\mathrm{H_2,w}}$ denotes the solubility of hydrogen in pure water, calculated using the following equation:

$$S_{\mathrm{H_2,w}} = 0.54 \exp\left(-48.1611 + \frac{5528.45}{T} + 16.8893 \ln\left(\frac{T}{100}\right)\right) \tag{8}$$

The term $S_{\mathrm{r,diss}}$ in Eq. (1) represents the mass source for dissolved $\mathrm{H_2}$ consumption due to HOR in the CCL, calculated using the following equation [43]:

$$S_{\mathrm{r,diss}} = \frac{J_{\mathrm{cross}}}{2F} \tag{9}$$

where J_{cross} denotes the volumetric current density generated by HOR in the CCL, and F is the Faraday constant.

The term S_{ml} in Eq. (4) represents the mass source for the liquid mixture in the membrane, accounting for water adsorption from the gas phase to the membrane phase, H_2 dissolution, and dissolved H_2 consumption by HOR processes, calculated using the following equations:

$$S_{\mathrm{ml}} = \begin{cases} S_{\mathrm{v-d}} M_{\mathrm{H_2O}} + \left(S_{\mathrm{H_2,diss}} - S_{\mathrm{r,diss}}\right) M_{\mathrm{H_2}} (\mathrm{cCL}) \\ S_{\mathrm{v-d}} M_{\mathrm{H_2O}} + S_{\mathrm{H_2,diss}} M_{\mathrm{H_2}} (\mathrm{aCL}) \end{cases} \tag{10}$$

where $S_{\mathrm{v-d}}$ denotes the quantity of gaseous water adsorbed by ionomers; calculation of this term follows equations presented in our previous work [41].

This concludes the dissolved hydrogen equation group. The resulting crossover current density J_{cross} (Eq. (9)) feeds into the charge transport (Section 3.2.5) and energy transport (Section 3.2.6) equation groups as a source term.

3.2.2 Mixture Gas Transport

This subsection presents the gas-phase mixture equation group (Eqs. (11)–(13)), governing the overall mass conservation of the gas mixture in gas channels and porous media.

The mass conservation equation of gas mixture in GCs, GDLs, MPLs, and CLs is solved as follows [39]:

$$\frac{\partial}{\partial t}\left(\varepsilon(1-s)\rho_{\mathrm{g}}\right) + \nabla \cdot \rho_{\mathrm{g}} \boldsymbol{u}_{\mathrm{g}} = S_{\mathrm{g}} \tag{11}$$

where ρ_{g} denotes the density of the gas mixture; $\boldsymbol{u}_{\mathrm{g}}$ is the velocity of the gas mixture, obtained using Darcy's law [39,47]; S_{g} represents the mass source; ε is the volumetric porosity of porous materials; and s is the liquid water saturation.

In Eq. (11), the source terms S_{g} denoted as represent mass consumption and generation during phase transitions and electrochemical reactions. Within the ACL, these terms account for H_2 consumption through HOR, H_2 dissolution from the gas phase into the ionomer, as well as water condensation and adsorption. The calculations are detailed as follows:

$$S_{\mathrm{g}} = -\frac{J_{\mathrm{a}}}{2F} M_{\mathrm{H_2}} - M_{\mathrm{H_2O}} S_{\mathrm{v-l}} - M_{\mathrm{H_2O}} S_{\mathrm{v-d}} - M_{\mathrm{H_2}} S_{\mathrm{H_2,diss}} \tag{12}$$

where J_{a} represents the volumetric current density of HOR at the anode; M is the molar mass; and $S_{\mathrm{v-l}}$ indicates the amount of gaseous water condensing into liquid water in pores, as detailed in our previous work [41].

Within the CCL, these terms account for water generation and O_2 consumption by ORR, water phase transitions between gas-liquid-membrane phases, and H_2 dissolution from pores into ionomer. The calculations are shown as follows:

$$S_{\mathrm{g}} = \frac{J_{\mathrm{c}}}{2F} M_{\mathrm{H_2O}} - \frac{J_{\mathrm{c}}}{4F} M_{\mathrm{O_2}} - M_{\mathrm{H_2O}} S_{\mathrm{v-l}} - M_{\mathrm{H_2O}} S_{\mathrm{v-d}} - M_{\mathrm{H_2}} S_{\mathrm{H_2,diss}} \tag{13}$$

where J_{c} is the volumetric current density at the cathode.

This concludes the mixture gas equation group. The mass source terms S_{g} couple this group to the electrochemical reaction kinetics (Section 3.3) and the dissolved hydrogen transport (Section 3.2.1).

3.2.3 Gas Species Transport

This section presents the gas species transport equation group (Eqs. (14)–(19)), tracking individual components (H_2, O_2, N_2, and H_2O) via convection-diffusion equations.

The mass conservation of gas species in GCs, GDLs, MPLs, and CLs is solved as follows [41]:

$$\frac{\partial}{\partial t}\left(\varepsilon\left(1-s\right)C_{\mathrm{i}}\right)+\nabla\cdot\left(C_{\mathrm{i}}\boldsymbol{u}_{\mathrm{g}}\right)+\nabla\cdot\left(-D_{\mathrm{i}}^{\mathrm{eff}}\nabla C_{\mathrm{i}}\right)=S_{\mathrm{i}} \tag{14}$$

where C_{i} is the gas species concentration; $D_{\mathrm{i}}^{\mathrm{eff}}$ denotes the effective diffusion coefficient, calculated as detailed in our previous work [41]; and S_{i} represents the source terms due to electrochemical reactions and phase transitions, with values varying by species. At the anode, species i can be H_2 or H_2O, while at the cathode, species may include O_2, H_2, N_2, and H_2O.

The source terms for H_2 and H_2O species in the ACL account for H_2 consumption by HOR, H_2 dissolution into ionomer, and water phase transitions, as outlined below.

$$S_{\mathrm{H_2}}=-\frac{J_{\mathrm{a}}}{2F}-S_{\mathrm{H_2,diss}} \tag{15}$$

$$S_{\mathrm{H_2O}}=-S_{\mathrm{v-l}}-S_{\mathrm{v-d}} \tag{16}$$

The source terms for O_2, H_2, and H_2O in the CCL account for O_2 consumption by ORR, H_2 dissolution into ionomer, H_2O generation by ORR, and water phase transitions between gas-liquid-membrane phases, as given below.

$$S_{\mathrm{O_2}}=-\frac{J_{\mathrm{c}}}{4F} \tag{17}$$

$$S_{\mathrm{H_2}}=-S_{\mathrm{H_2,diss}} \tag{18}$$

$$S_{\mathrm{H_2O}}=\frac{J_{\mathrm{c}}}{2F}-S_{\mathrm{v-l}}-S_{\mathrm{v-d}} \tag{19}$$

This concludes the species transport equation group. The species fluxes provide boundary conditions for the dissolved hydrogen equation group (Section 3.2.1) via Henry's law.

3.2.4 Liquid and Membrane Water Transport

This section comprises the water transport equation group (Eqs. (20) and (21)), addressing liquid water in porous media and membrane water governed by diffusion and electro-osmotic drag.

The mass conservation of liquid water in GDLs, MPLs, and CLs is governed by the following equation [48]:

$$\frac{\partial}{\partial t}\left(\varepsilon s\rho_{\mathrm{l}}\right)+\nabla\cdot\rho_{\mathrm{l}}\boldsymbol{u}_{\mathrm{l}}=S_{\mathrm{l}} \tag{20}$$

where ρ_{l} represents the density of liquid water; $\boldsymbol{u}_{\mathrm{l}}$ denotes the velocity of liquid water, determined by Darcy's law [39,47]; and S_{l} represents the mass source term resulting from water condensation, calculated as $M_{\mathrm{H_2O}}S_{\mathrm{v-l}}$.

The transport of membrane water in CLs and PEM involves two key mechanisms: membrane water diffusion driven by concentration gradients and electro-osmotic drag driven by potential gradients. The mass conservation equation is given as follows [41]:

$$\frac{\partial}{\partial t}(\varepsilon_{\mathrm{m}} C_{\mathrm{m}}) + \nabla \cdot \left(-D_{\mathrm{m}}^{\mathrm{eff}} \nabla C_{\mathrm{m}} - \frac{n_{\mathrm{d}}}{F} \sigma_{\mathrm{m}}^{\mathrm{eff}} \nabla \phi_{\mathrm{m}}\right) = \mathrm{S}_{\mathrm{v-d}} \tag{21}$$

where C_{m} is the concentration of membrane water in the membrane; $D_{\mathrm{m}}^{\mathrm{eff}}$ is the effective diffusion coefficient; n_{d} is the electro-osmotic drag coefficient; $\sigma_{\mathrm{m}}^{\mathrm{eff}}$ is the effective proton conductivity; ϕ_{m} is the proton potential; and $S_{\mathrm{v-d}}$ represents the mass source term for water adsorption by the ionomer. The methods for calculating these physical and transport parameters have been detailed in our previous work [41].

This concludes the water transport equation group. The membrane water content (characterized by the water volume fraction f_{v} in Eq. (2)) directly modifies the diffusion coefficient in the dissolved hydrogen equation group.

3.2.5 Charge Transport

This section presents the charge transport equation group (Eqs. (22)–(25)), describing proton and electron conduction via Ohm's law.

The charge balance of electrons in BPs, GDLs, MPLs, and CLs, and protons in CLs and PEM, follows Ohm's law and is determined using the following equation [41].

$$\nabla \cdot (-\sigma_{\mathrm{m}}^{\mathrm{eff}} \nabla \phi_{\mathrm{m}}) = S_{\mathrm{H}} \tag{22}$$

$$\nabla \cdot (-\sigma_{\mathrm{e}}^{\mathrm{eff}} \nabla \phi_{\mathrm{e}}) = S_{\mathrm{e}} \tag{23}$$

where $\sigma_{\mathrm{e}}^{\mathrm{eff}}$ denotes the effective electron conductivity; ϕ_{e} is the electronic potential; and S_{H} and S_{e} are the source terms for protons and electrons, respectively.

The proton source in the aCL is derived from HOR, which generates protons. In contrast, the proton source in cCL includes proton consumption during ORR and proton production from permeated H_2 via HOR. The calculation equation is given as follows:

$$S_{\mathrm{H}} = \begin{cases} J_{\mathrm{a}} & (\mathrm{aCL}) \\ -J_{\mathrm{c}} + J_{\mathrm{cross}} & (\mathrm{cCL}) \end{cases} \tag{24}$$

The electron source in the aCL is attributed to electron generation from HOR. In contrast, the electron source in the cCL encompasses both electron consumption during ORR and electron generation from HOR due to H_2 crossover.

$$S_{\mathrm{e}} = \begin{cases} -J_{\mathrm{a}} & (\mathrm{aCL}) \\ J_{\mathrm{c}} - J_{\mathrm{cross}} & (\mathrm{cCL}) \end{cases} \tag{25}$$

This concludes the charge transport equation group. The current densities J_{a} and J_{c} serve as source terms for the gas-phase and energy equation groups.

3.2.6 Energy Transfer

This section presents the energy transport equation group (Eqs. (26) and (27)), governing heat conduction, convection, and generation within the cell, including the reversible and irreversible heat released by hydrogen crossover at the cathode.

The energy conservation in GDLs, MPLs, and CLs is addressed using the following equation, which incorporates energy transport mechanisms such as heat conduction, diffusion, and convection [41].

$$\frac{\partial}{\partial t}\left((1-\varepsilon)\,\rho_s C_{p,s} T + \varepsilon s \rho_l C_{p,l} T + \varepsilon\,(1-s)\,\rho_g C_{p,g} T\right) + \nabla\cdot\left(-k^{eff}\nabla T\right) + \nabla\cdot\left(\sum_i \left(-D_i^{eff}\nabla C_i\right) M_i C_{p,\,i} T\right) + \nabla\cdot\left(\rho_l \mathbf{u}_l C_{p,l} T + \rho_g \mathbf{u}_g C_{p,g} T\right) = S_T \tag{26}$$

where ρ denotes density, C_p represents specific heat capacity, and T is temperature. The term k^{eff} refers to effective thermal conductivity, while subscripts s, g, and l denote solid, gaseous, and liquid phases, respectively. Additionally, S_T represents the heat source, accounting for heat release associated with phase transitions, proton and electron conduction, and electrochemical reactions in CLs. Notably, the newly introduced reversible and irreversible heat source terms caused by HOR due to H_2 crossover in the CCL are included, as shown in the following equation:

$$S_T = \begin{cases} \sigma_e^{eff} + \sigma_m^{eff}\nabla\phi_m{}^2 + J_a\left(\phi_{eq,a} - \dfrac{-\Delta H_{hor}}{2F}\right) + J_a\eta_a + S_T^{v-l} + S_T^{v-d} & \text{(aCL)} \\ \sigma_e^{eff}\nabla\phi_e{}^2 + \sigma_m^{eff}\nabla\phi_m{}^2 - J_c\left(\phi_{eq,c} - \dfrac{-\Delta H_{orr}}{2F}\right) - J_c\eta_c + S_T^{v-l} + S_T^{v-d} + J_{cross}\left(\phi_{eq,a} - \dfrac{-\Delta H_{hor}}{2F}\right) + J_{cross}\eta_{cross} & \text{(cCL)} \end{cases} \tag{27}$$

where $\phi_{eq,a}$ and $\phi_{eq,c}$ represent the equilibrium potentials for HOR and ORR, respectively. ΔH_{hor} and ΔH_{orr} denote the enthalpy changes associated with HOR and ORR, respectively. Additionally, η_a, η_c and η_{cross} represent the overpotentials for HOR at the anode, ORR at the cathode, and HOR at the cathode, respectively. S_T^{v-l} and S_T^{v-d} represent the heat associated with phase changes of water, as detailed in our previous work. $J_{cross}\left(\phi_{eq,a} - \frac{-\Delta H_{hor}}{2F}\right)$ is the reversible heat for HOR at the cathode, while $J_{cross}\eta_{cross}$ is the irreversible heat for HOR at the cathode.

This concludes the energy transport equation group. The resulting temperature field affects the hydrogen diffusion coefficient in Section 3.2.1 via the Arrhenius relation (Eq. (3)), closing the thermal-hydrogen coupling loop.

3.3 Reaction Kinetics

This section presents the electrochemical kinetics equation group (Eqs. (28)–(33)), defining reaction rates and overpotentials via Butler-Volmer equations for HOR and ORR.

As shown in Fig. 1c, the anode exclusively facilitates HOR, with reaction kinetics characterized by the Butler-Volmer equation [49]:

$$J_a = i_{0,a}^{ref} a_{Pt} \exp\left[-1400\left(\frac{1}{T} - \frac{1}{353.15}\right)\right]\left(\frac{C_{H_2}}{C_{H_2}^{ref}}\right)\left[\exp\left(\frac{F}{RT}\eta_a\right) - \exp\left(-\frac{F}{RT}\eta_a\right)\right] \tag{28}$$

where i_0^{ref} is the reference exchange current density; a_{Pt} is the electrocatalytic surface area per unit volume; and C_i^{ref} denotes the reference molar concentration.

At the cathode, both ORR and HOR coexist due to H_2 permeation. The ORR rate is described by the Butler-Volmer equation, given as follows:

$$J_c = i_{0,c}^{ref} a_{Pt} \exp\left[-7900\left(\frac{1}{T} - \frac{1}{353.15}\right)\right]\left(\frac{C_{O_2}}{C_{O_2}^{ref}}\right)\left[\exp\left(\frac{3F}{RT}\eta_c\right) - \exp\left(-\frac{F}{RT}\eta_c\right)\right] \tag{29}$$

The HOR rate at the cathode is sufficiently high due to the high electrode potential, and is solved using the following equation [23]:

$$J_{\mathrm{cross}} = i_{0,\mathrm{a}}^{\mathrm{ref}} a_{\mathrm{Pt}} \frac{C_{\mathrm{H_2,diss}}}{C_{\mathrm{H_2}}^{\mathrm{ref}}} \exp\left[-1400\left(\frac{1}{T} - \frac{1}{353.15}\right)\right]\left[\exp\left(\frac{F}{RT}\eta_{\mathrm{cross}}\right) - \exp\left(-\frac{F}{RT}\eta_{\mathrm{cross}}\right)\right] \tag{30}$$

where η_{cross} is the overpotential for the HOR inside the cCL.

The above-mentioned three overpotentials are solved using:

$$\eta_{\mathrm{a}} = \phi_{\mathrm{e}} - \phi_{\mathrm{m}} \tag{31}$$

$$\eta_{\mathrm{c}} = \phi_{\mathrm{e}} - \phi_{\mathrm{m}} - \phi_{\mathrm{eq,c}} \tag{32}$$

$$\eta_{\mathrm{cross}} = \phi_{\mathrm{e}} - \phi_{\mathrm{m}} \tag{33}$$

where ϕ_{e} and ϕ_{m} are the electric potential and the ionic potential, respectively, ϕ_{eq} is the equilibrium potential.

This concludes the kinetics equation group. These current densities close the coupling loop by serving as source terms for the charge (Section 3.2.5), mass (Sections 3.2.1–3.2.3), and energy (Section 3.2.6) conservation equations.

3.4 Boundary Conditions

This section defines the boundary condition equation group (Eqs. (34)–(37)), specifying inlet stoichiometric flows, concentrations, and interfacial flux conditions.

The primary boundary conditions are as follows: the outlet pressures of both the anode and cathode are fixed to the respective backing pressures. The inlet flow rates of the gas mixtures on both the cathode and anode sides are determined by solving:

$$\boldsymbol{u}_{\mathrm{a}} = \xi_{\mathrm{a}} \frac{I(\mathrm{t}) A_{\mathrm{m}}}{2FA_{\mathrm{ch}} C_{\mathrm{H_2}}} \tag{34}$$

$$\boldsymbol{u}_{\mathrm{c}} = \xi_{\mathrm{c}} \frac{I(\mathrm{t}) A_{\mathrm{m}}}{4FA_{\mathrm{ch}} C_{\mathrm{O_2}}} \tag{35}$$

where ξ denotes the stoichiometric ratios of H_2 at the anode and O_2 at the cathode, $I(\mathrm{t})$ represents the time-varying current load, A_{m} denotes the area of the membrane-electrode assembly parallel to the flow channel direction, and A_{ch} represents the cross-sectional area of the flow channel. Additionally, $C_{\mathrm{H_2}}$ and $C_{\mathrm{O_2}}$ denote the concentrations of hydrogen and oxygen at the inlet, respectively, and are expressed as:

$$C_{\mathrm{H_2}} = \frac{p_{\mathrm{g,a}} - RH_{\mathrm{a}} \times p_{\mathrm{sat}}}{RT} \tag{36}$$

$$C_{\mathrm{O_2}} = 0.21\left(\frac{p_{\mathrm{g,c}} - RH_{\mathrm{c}} \times p_{\mathrm{sat}}}{RT}\right) \tag{37}$$

where p_{g}, RH and p_{sat} are the gas pressures at the inlets, the relative humidities, and the saturation vapor pressure, respectively.

Furthermore, the pressure of the liquid mixture p_{ml} at the interface between the MPL and CL within the electrolyte is set to be in equilibrium with the liquid pressure. The H_2 crossover flux ($\boldsymbol{u}_{\mathrm{H_2,diss}} C_{\mathrm{H_2,diss}} - D_{\mathrm{H_2,diss}} \nabla C_{\mathrm{H_2,diss}}$) is maintained at zero at the MPL|CL interface. These boundary conditions drive the transient response of all preceding equation groups.

4 Results and Discussion

4.1 Model Implementation and Verification

The computational model was analyzed using COMSOL 6.1. Fig. 3a illustrates the outcomes of the independence test regarding the number of elements. This evaluation was performed under high current densities ranging from 1800 to 2000 mA cm^{-2}, reflecting the rigorous requirements for element quality at these elevated current levels. Notably, when the element count exceeds 14,000, the model demonstrates a nearly constant voltage prediction trend as the number of elements increases. To achieve an optimal balance between computational accuracy and time efficiency, the final selected number of elements is established at 14,000. Fig. 3b,c presents a comparison of model-predicted data with experimentally measured data. The experimental conditions were meticulously aligned with the simulation parameters, which included a temperature of 90°C, backing pressures of 130 kPa at the anode and 120 kPa at the cathode, stoichiometric ratios of 1.7 at the anode and 3.0 at the cathode, and a relative humidity of 0.5 at both the anode and cathode. Additionally, the membrane thickness was set at 8 μm. Fig. 3b illustrates the correlation between the steady-state polarization curves obtained from the 3D model and the experimental data, demonstrating a maximum error of 2%. In Fig. 3c, a significant correlation is observed in the transient cell voltage response under a step load condition, with a current step from 600 to 1600 mA cm^{-2} applied between 2 and 3 s, with an error margin also below 2%. Both the simulations and experiments effectively capture the undershoot voltage of approximately 0.01 V, which can be attributed to instantaneous local oxygen starvation and low levels of membrane hydration. This validation relies on global performance metrics (steady-state polarization and transient voltage), which is widely adopted in the literature to establish model credibility before extending predictions to local phenomena [27,50].

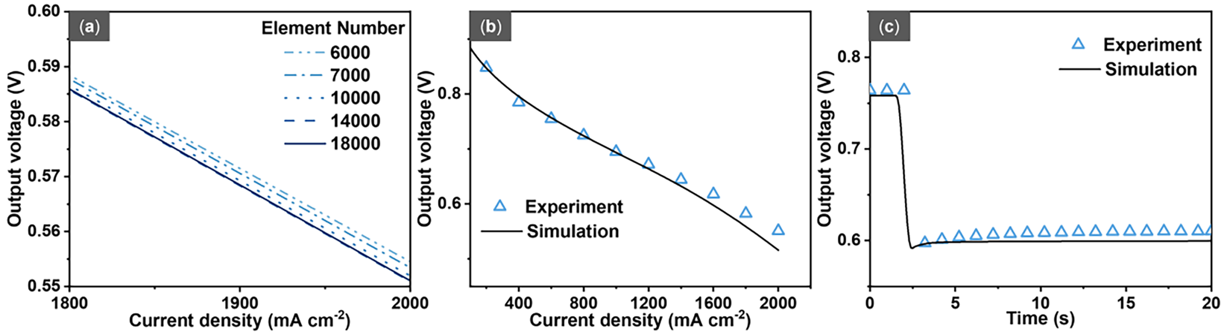

Figure 3: Model validation under 90°C, 130/120 kPa (anode/cathode), 50% RH, stoichiometric ratios of 1.7/3.0 with 8 μm membrane: (**a**) Mesh independence test at 1800–2000 mA cm^{-2} showing convergence at 14,000 elements; (**b**) Steady-state polarization curve comparison between simulation and experiment (maximum error of 2%); (**c**) Transient voltage response under step load from 600 to 1600 mA cm^{-2} from 2 to 3 s over 1 s, showing ~0.01 V undershoot (error below 2%).

Fig. 4a presents a comparative analysis of the model results with and without considering the impact of H_2 crossover on fuel cell performance, mass transfer, and heat transfer. The findings indicate that neglecting H_2 crossover leads to a substantial overestimation of the output voltage, particularly the open circuit voltage (OCV). Specifically, the OCV is 0.972 V when H_2 crossover effects are accounted for, while it rises to 1.182 V when these effects are ignored, resulting in a difference of 210 mV. This discrepancy is attributed to the formation of localized H_2-O_2 fuel cells, aligning with the simulation results reported by Vilekar and Datta [23]. However, the influence of these localized fuel cells diminishes notably with increasing load, as their effect on electrode potential decreases [22]. Additionally, when H_2 crossover effects are not considered, the cell average temperature is underestimated by approximately 0.2°C across the entire current density range. This increase in temperature observed with H_2 crossover is primarily due to the additional heat generated during the HOR and ORR at the cathode [50]. Fig. 4b further presents a comparison between the H_2 crossover current density predicted by the model and the experimental data under identical operating conditions: a Nafion 112 membrane with a thickness of 50 μm, at 80°C, with saturated gases, and at OCV. The model predictions demonstrate excellent agreement with the experimental data, illustrating a consistent trend where the H_2 crossover current increases with the rise in H_2 partial pressure on the anode side. This correlation emphasizes the accuracy of the model in capturing the effects of H_2 crossover under specified conditions.

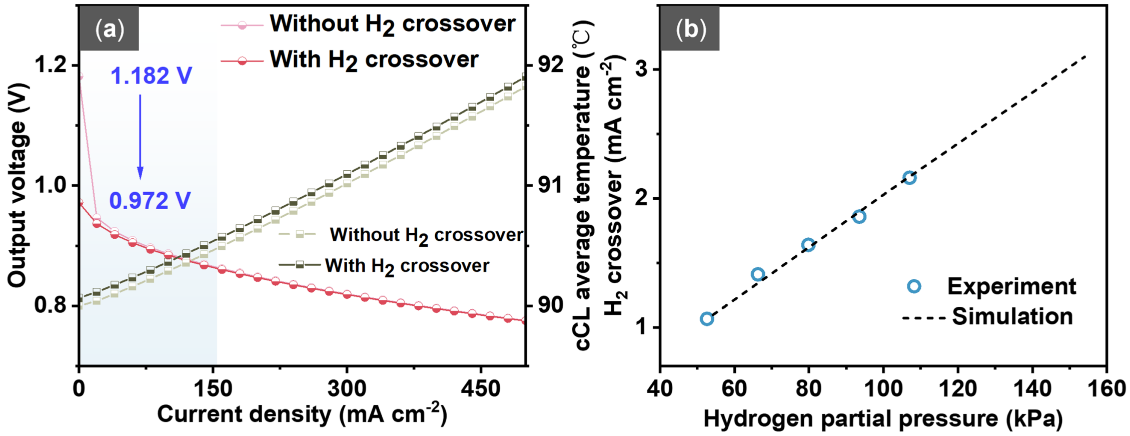

Figure 4: Impact of H_2 crossover on fuel cell performance and model validation: (**a**) Comparison of output voltage and cCL average temperature with and without H_2 crossover (OCV reduction of 210 mV from 1.182 to 0.972 V, and ~0.2°C temperature increase when crossover is considered); (**b**) Validation of H_2 crossover current density vs. anode H_2 partial pressure under Nafion 112, 50 μm thickness, 80°C, saturated gases, OCV conditions (simulation vs. experimental data [15]).

4.2 Effect of Membrane Thickness

The influence of membrane thickness on fuel cell performance and the concentration of dissolved H_2 under dynamic load conditions is illustrated in Fig. 5. Specifically, Fig. 5a demonstrates a significant reduction in the output voltage of the fuel cell as the current load increases rapidly from 10 to 1800 mA cm^{-2} between 9.9 and 10.1 s (within 0.2 s), which is accompanied by a notable voltage undershoot. Fig. 5b shows that after 30 s, the voltage decreases from 0.59 to 0.55, 0.52, and 0.49 V as the thickness of the PEM is increased from 5 to 10, 15, and 20 μm, respectively. Correspondingly, the voltage undershoots, defined as the difference between the voltage at 30 s and the minimum value observed at 10 s, increases to 0.013 0.024, and 0.036 V from a baseline of 0.004 V, respectively.

These results suggest a heightened power loss during both steady-state and dynamic operations, which can be attributed to the increased proton-conducting resistance associated with thicker membranes. Furthermore, it is critical to note that the thickness of the PEM not only impacts the performance of the fuel cell but also induces variations in internal H_2 crossover.

Fig. 5c illustrates the dynamic responses of dissolved H_2 concentration within the PEM, and shows that the steady-state dissolved H_2 concentration exhibits a positive correlation with the thickness of the PEM, with a thicker membrane facilitating higher concentrations. Additionally, an undershoot phenomenon is observed for dissolved H_2 concentration when the load undergoes rapid increases, with slight variations depending on the PEM thickness, as depicted in Fig. 5d.

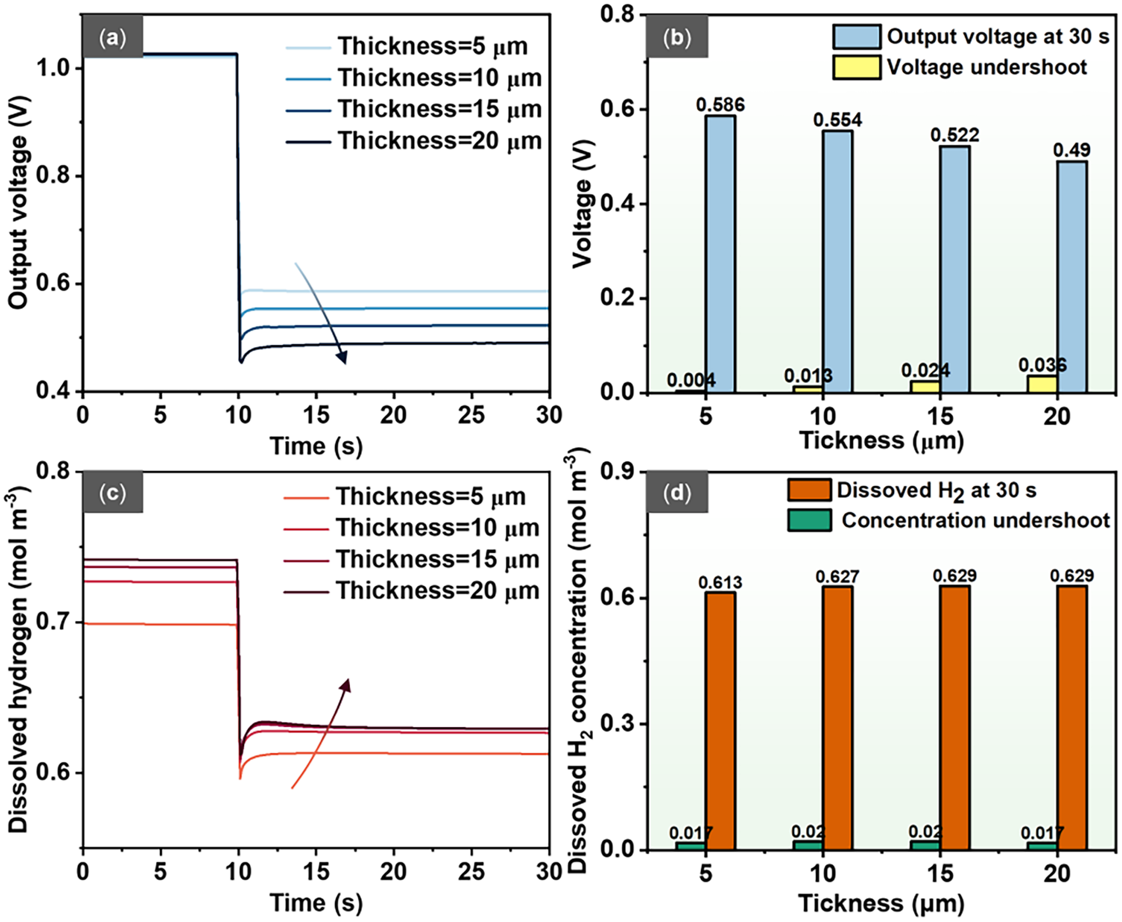

Figure 5: Effect of membrane thickness on fuel cell dynamic performance under a step load change from 10 to 1800 mA cm^{-2} within 0.2 s (from 9.9 s to 10.1 s) with total simulation time of 30 s, operating conditions: 90°C, 130/120 kPa (anode/cathode), 50% RH: (**a**) Dynamic response of output voltage from 9.9 s to 10.1 s for PEM thicknesses of 5, 10, 15, and 20 μm; (**b**) Variations of voltage undershoot and steady-state voltage at 30 s with PEM thickness; (**c**) Dynamic responses of dissolved H_2 concentration at the anode–PEM interface for PEM thicknesses of 5, 10, 15, and 20 μm; (**d**) Variations of dissolved H_2 concentration undershoot and steady-state concentration at 30 s with PEM thickness.

The undershoot in dissolved H_2 concentration can be attributed to the dynamic interplay of local H_2 gas concentration, temperature, and membrane water content. Fig. 6a clearly demonstrates that as the load increases, there is a rapid decrease in H_2 gas concentration within the aCL, leading to a significant decline in the dissolved H_2 concentration, as observed in Fig. 5c. This decline is governed by the proportional relationship between H_2 gas partial pressure and the saturated dissolved H_2 concentration, as described by Eq. (7). However, over time, the dissolved H_2 concentration gradually increases, eventually reaching a new steady state, which gives rise to the undershoot phenomenon. Notably, the H_2 gas concentration within the aCL remains relatively constant during this process. The gradual increase in dissolved H_2 can be attributed to enhanced H_2 crossover resulting from increased local membrane water content and temperature, which facilitate H_2 dissolution and permeation through the membrane.

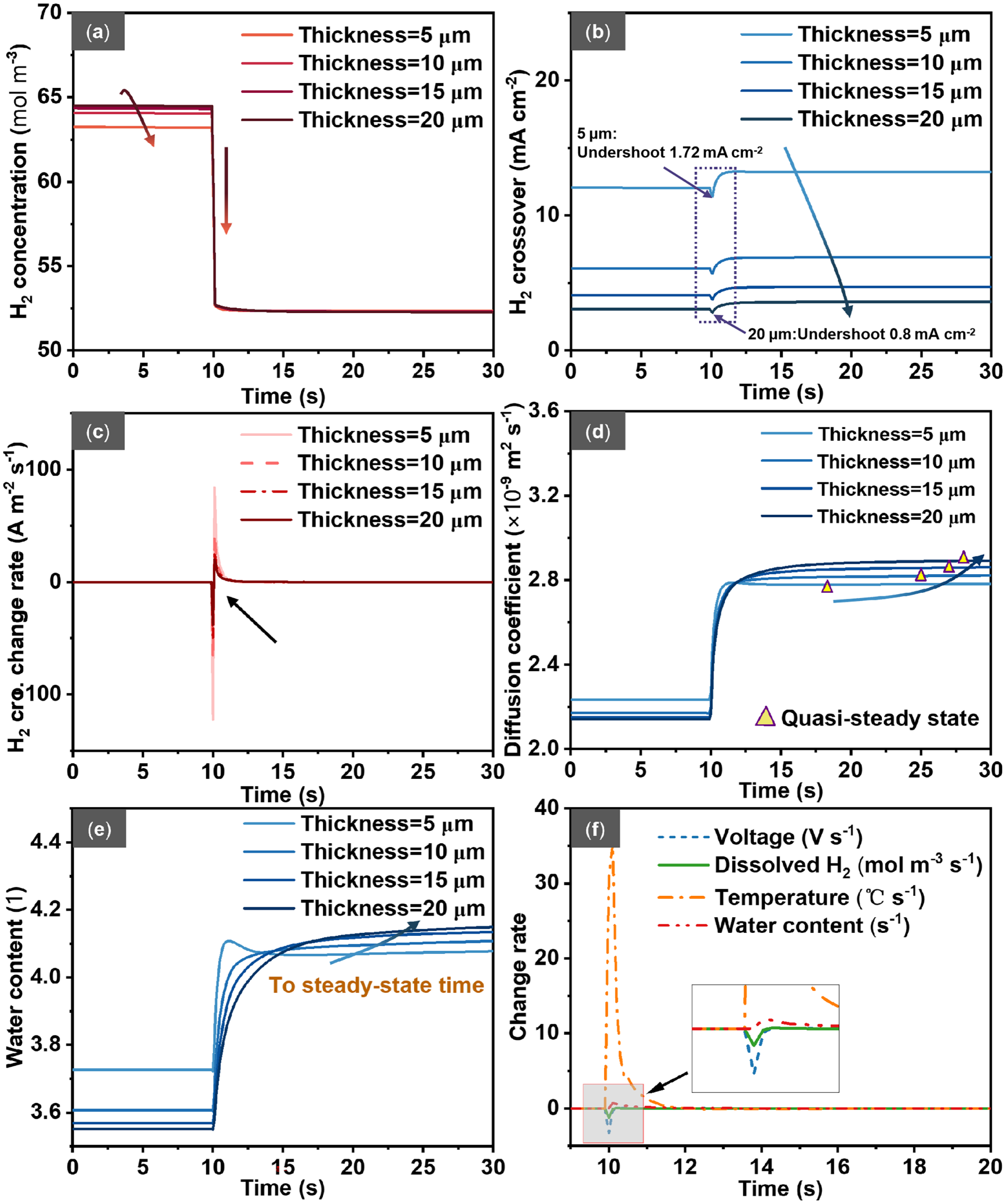

Figure 6: Dynamic response mechanisms of hydrogen transport and membrane properties under a step load from 10 to 1800 mA cm^{-2} within 0.2 s (from 9.9 s to 10.1 s) at 90°C, 130/120 kPa (anode/cathode), 50% RH for various PEM thicknesses (5–20 μm): (**a**) Average H_2 gas concentration in the anode catalyst layer; (**b**) H_2 crossover current density through the PEM; transient minima and post-step recovered values are approximately 2.8 and 3.6 mA cm^{-2} for the 20 μm membrane, and 11.4 and 13.2 mA cm^{-2} for the 5 μm membrane, respectively; the undershoot, defined as the difference between the post-step recovered value and the transient minimum, ranges from approximately 0.8 mA cm^{-2} for the 20 μm membrane to 1.72 mA cm^{-2} for the 5 μm membrane; (**c**) Change rate of H_2 crossover current density; (**d**) Diffusion coefficient of dissolved H_2; (**e**) Water content in the PEM; (**f**) Comparative change rates of fuel cell voltage, dissolved H_2 inside PEM, PEM temperature, and PEM water content illustrating the temporal sequence of transient responses.

As shown in Fig. 6b, the H_2 crossover current density through the PEM demonstrates an almost fourfold reduction as the PEM thickness increases from 5 to 20 μm. For the 5 μm membrane, the H_2 crossover current density decreases to a transient minimum of approximately 11.4 mA cm^{-2} and subsequently recovers to approximately 13.2 mA cm^{-2}. For the 20 μm membrane, the corresponding transient minimum and post-step recovered value are approximately 2.8 and 3.6 mA cm^{-2}, respectively. This substantial decrease can be ascribed to the longer transport pathways and the greater transport resistance inherent to thicker membranes, which hinder the transfer of dissolved H_2 from the aCL to the cathode. Moreover, this phenomenon also results in a decrease in the rate of change of H_2 crossover with increasing thickness of the PEM. From the perspective of diffusion mechanisms regulating H_2 crossover, a thicker membrane creates a longer diffusion path, which consequently delays the changes in H_2 crossover [28,33,51]. Additionally, when examining the rate of change of H_2 crossover in relation to varying loads, Fig. 6c illustrates that the change rate initially follows a negative trajectory and then shifts to a positive trend as the load increases. This pattern is consistent with the H_2 crossover current density presented in Fig. 6b, where an initial decline is observed, followed by a notable increase around the 10-s mark. The resulting undershoot, defined as the difference between the post-step recovered value and the transient minimum, ranges from approximately 0.8 mA cm^{-2} for the 20 μm membrane to 1.72 mA cm^{-2} for the 5 μm membrane.

The initial decrease can be attributed to a diminishing gradient of dissolved H_2 from the anode to the cathode. Conversely, the subsequent increase is linked to an enhanced diffusion coefficient, which arises from the hydration of the membrane, as illustrated in Fig. 6d. The increase in PEM thickness leads to a longer time for the diffusion coefficient in Fig. 6d to reach a new steady state. This delay can be attributed to the slower evolution of membrane water, as observed in Fig. 6e. The rates of change of voltage, dissolved H_2, local temperature, and water content are summarized in Fig. 6f. The results indicate that the output voltage exhibits the fastest response, followed by dissolved H_2, membrane water, and temperature. This suggests that the dynamic response of dissolved H_2 is faster compared to heat and water transfer.

Fig. 7 presents the 3D distributions of dissolved H_2, H_2 crossover, and water content within a 15 μm PEM during load steps. As the load increases from 9.9 s to 10 s, the dissolved H_2 near the aCL decreases noticeably, which is attributed to the rapid decline in H_2 gas concentration inside the aCL. This decrease in dissolved H_2 concentration gradient from the anode to the cathode corresponds to a reduction in H_2 crossover flux from 4.0–4.1 to 3.5–4.0 mA cm^{-2}, as depicted in Fig. 7e,f. These findings are consistent with the average results shown in Figs. 5c and 6b. Between 10.1 s and 11 s, an increase in dissolved H_2 is observed in the inlet gas area adjacent to the anode side. This increase can be attributed to the elevated local temperature and the enhanced H_2 crossover flux, both of which facilitate a greater influx of H_2 gas from the aCL into the PEM. Over the same period, a significant increase in membrane water content is observed beneath the rib region, which primarily explains the rise in H_2 crossover from approximately 3.5–4.0 to 4.1–4.9 mA cm^{-2}. It is important to note that the expansion of Nafion clusters induced by water infiltration has previously been reported to enhance gas permeation [10,52,53].

At t = 10 s and 10.1 s, an unexpected increase in H_2 crossover is observed under the channel region, with values 0.1–0.7 mA cm^{-2} higher than those in the rib region, which contrasts with the trend in membrane water distribution. This variation can be attributed to the impact of the concentration gradient on H_2 crossover. During these time intervals, both the channel and rib regions exhibit low H_2 diffusion coefficient due to membrane dehydration. However, the intensified H_2 concentration gradient leads to an increased occurrence of H_2 crossover specifically in the channel region. As depicted in Fig. 7b,c, the dissolved H_2 concentration is notably higher under the channel region on the anode side, resulting in a localized concentration disparity that promotes a higher incidence of H_2 crossover in the channel region.

In contrast, at 11 s, the substantial increase in membrane water content beneath the rib region (Fig. 7l) correlates with a 0.1–0.4 mA cm^{-2} higher H_2 crossover relative to the channel region. This association is captured by the water-dependent diffusion coefficient (Eq. (2)) in the present continuum-scale formulation. While enhanced permeation in these hydrated regions is speculated based on the model results, it should be noted that the present macroscopic model does not explicitly resolve nanoscale structural features such as distinct water channel networks or ionic cluster morphology, consistent with the crossover distribution shown in Fig. 7h.

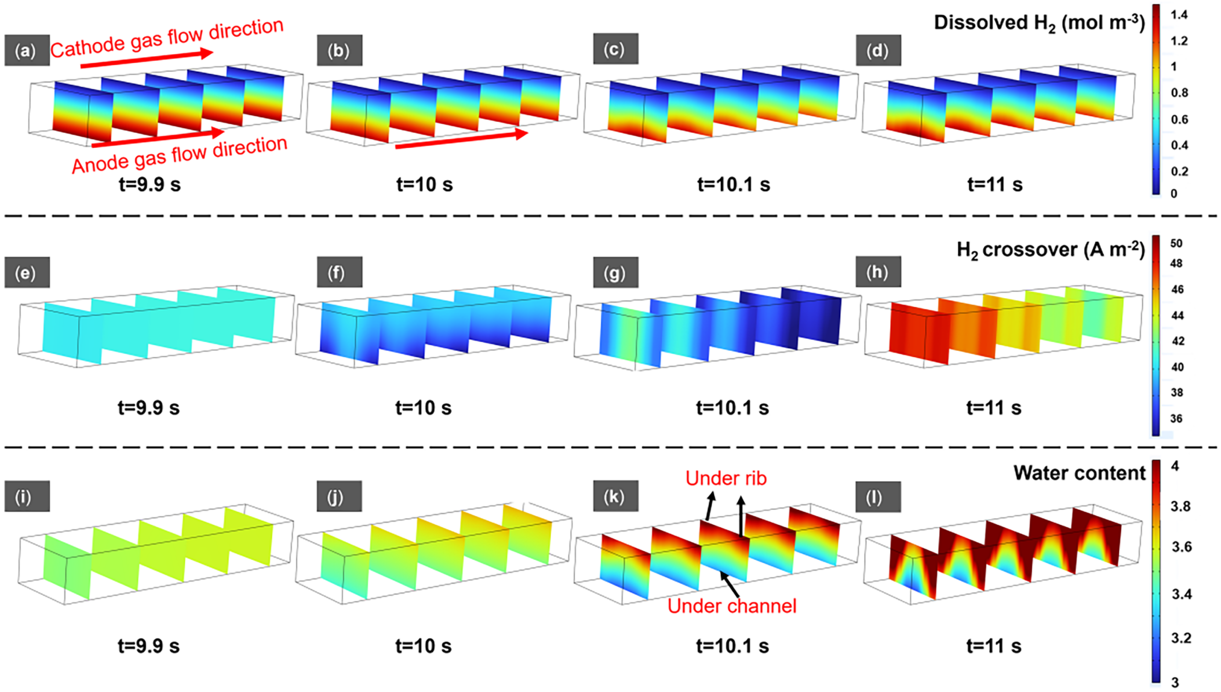

Figure 7: Transient spatial distributions within a 15 μm PEM during a step load change from 10 to 1800 mA cm^{-2} within 0.2 s (from 9.9 s to 10.1 s) at 90°C, 130/120 kPa (anode/cathode), and 50% RH, shown at critical moments (t = 9.9, 10, 10.1, and 11 s): (**a**–**d**) Dissolved H_2 concentration; (**e**–**h**) H_2 crossover flux; (**i**–**l**) Water content, illustrating the contrasting evolution between channel and rib regions during the load transient.

4.3 Effect of Stoichiometric Ratio

In this study, we investigate the impact of the anode stoichiometric ratio on H_2 crossover in a PEM fuel cell. The results presented in Fig. 8a demonstrate a significant increase in dissolved H_2 concentration within the PEM at higher anode stoichiometric ratios, particularly under high current loads. For instance, at a current density of 1800 mA cm^{-2} and 30 s, the dissolved H_2 concentrations are measured at 0.56, 0.60, 0.63, and 0.65 mol m^{-3} for H_2 stoichiometric ratios of 0.9, 1.3, 1.7, and 2, respectively (Fig. 8b).

This increase can be attributed to the elevated H_2 gas concentration within the aCL, as further supported by the data shown in Fig. S1. The amplified dissolved H_2 concentration further increases H_2 crossover flux and its dynamic undershoot. As shown in Fig. 8c, the H_2 crossover flux values at 10.1 s are 3.4, 3.63, 3.78, and 3.85 mA cm^{-2} for H_2 stoichiometric ratios of 0.9, 1.3, 1.7, and 2, respectively. Following the load change at 30 s, the increased dissolved H_2 at anode with stoichiometric ratio increases H_2 crossover with values of 4.27, 4.57, 4.73, and 4.81 mA cm^{-2}, respectively. This results in a more pronounced undershoot of H_2 crossover flux, with values of 0.87, 0.94, 0.95, and 0.96 mA cm^{-2}, respectively.

Fig. 8d further compares the change rates of H_2 crossover. As the anode stoichiometric ratio increases, the initial rate of decrease in H_2 crossover becomes less pronounced, while the subsequent rate of increase is markedly amplified. These trends can be attributed to the enhanced dissolved H_2 gradient between the anode and cathode. This increased gradient mitigates the transient decline in H_2 crossover resulting from the decrease in H_2 concentration, while simultaneously promoting the subsequent increase due to improved membrane hydration.

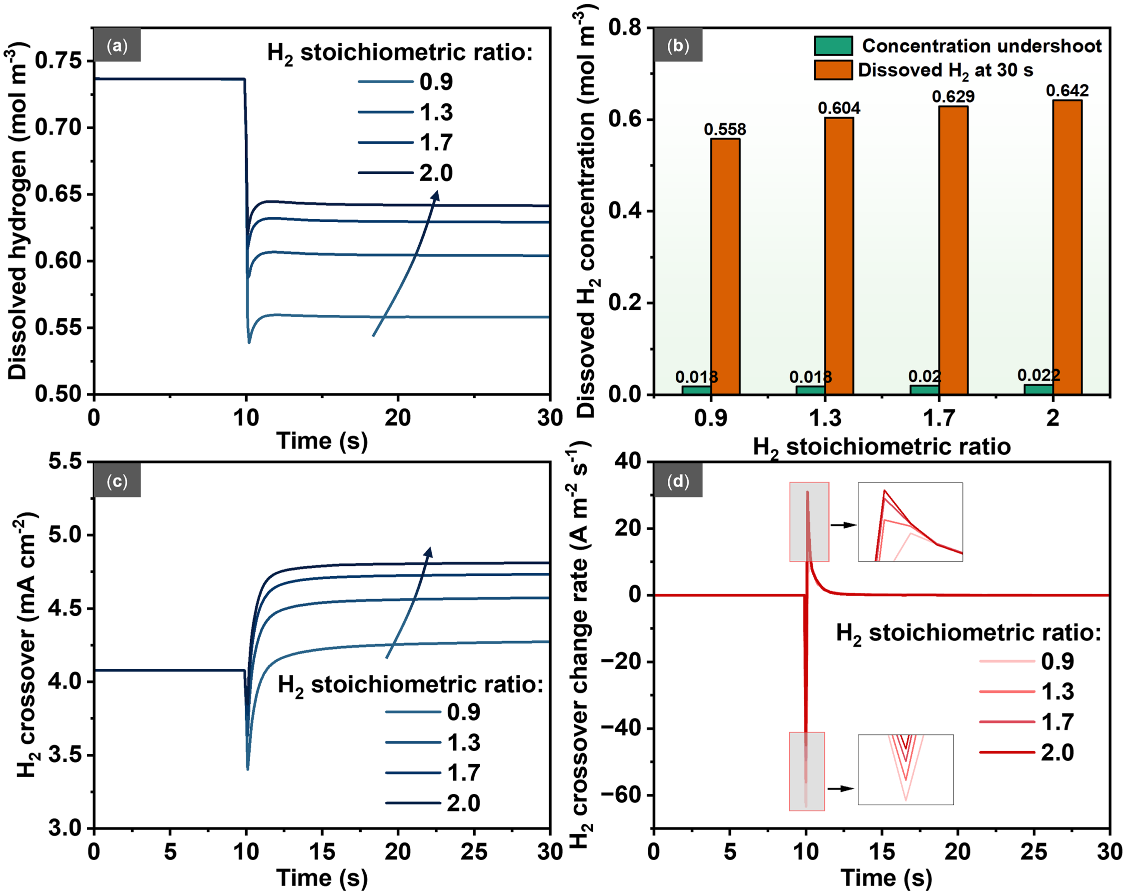

Figure 8: Effect of anode stoichiometric ratio (ξ_a = 0.9, 1.3, 1.7, 2) on hydrogen transport dynamics under a step load from 10 to 1800 mA cm^{-2} within 0.2 s (from 9.9 s to 10.1 s) at 90°C, 130/120 kPa (anode/cathode), and 50% RH: (**a**) Dynamic responses of dissolved H_2 concentration; (**b**) Dissolved H_2 concentration undershoot and steady-state values at 30 s; (**c**) Dynamic responses of H_2 crossover flux (values of 3.4–3.85 mA cm^{-2} at 10.1 s and 4.27–4.81 mA cm^{-2} at 30 s); (**d**) Change rates of H_2 crossover illustrating the transient undershoot phenomenon (0.87–0.96 mA cm^{-2}).

Fig. 9a–d illustrates the distribution of dissolved H_2 within the PEM at 10.1 s. The concentration of dissolved H_2 increases with the anode stoichiometric ratio, peaking in the region near the inlet on the anode side. This elevated concentration contributes to a larger area of high H_2 crossover within the PEM, as shown in Fig. 9e–h. The H_2 crossover flux varies across the anode stoichiometric ratios, ranging from 2.7–4.1 mA cm^{-2} for 0.9, 3.2–4.2 mA cm^{-2} for 1.3, 3.4–4.2 mA cm^{-2} for 1.7, and 3.5–4.3 mA cm^{-2} for 2. Notably, the channel region exhibits a more pronounced H_2 crossover due to a steeper H_2 concentration gradient. Additionally, H_2 crossover diminishes along with the gas flow direction, which can be attributed to the decrease in anode H_2 gas resulting from consumption during the electrochemical reaction.

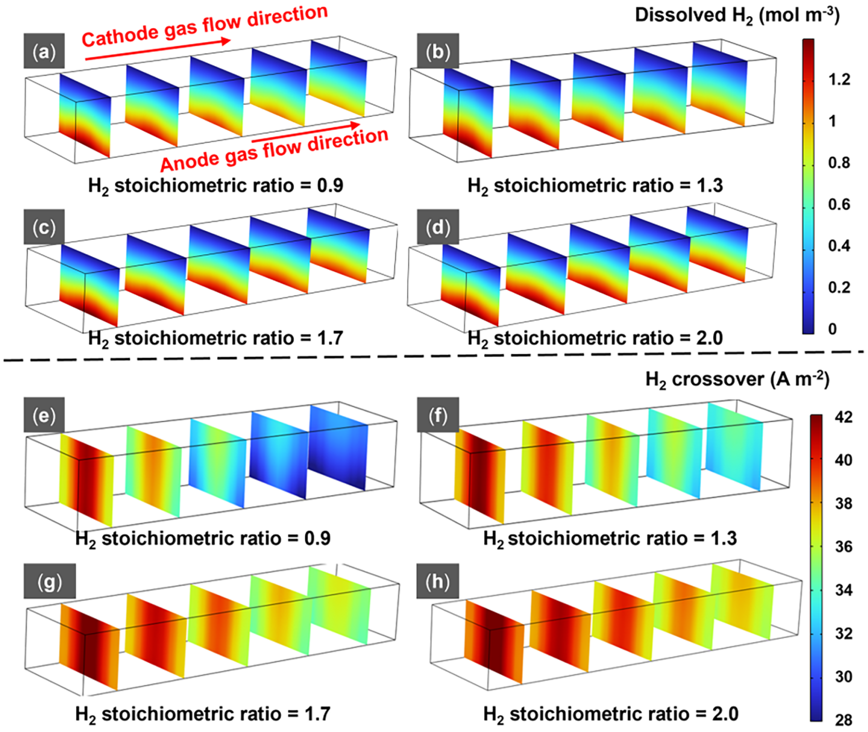

Figure 9: Spatial distributions of dissolved H_2 (**a–d**) and H_2 crossover flux (**e–h**) within the 15 μm PEM at t = 10.1 s as the current load increases from 10 to 1800 mA cm^{-2} at 90°C, 130/120 kPa, and 50% RH for anode stoichiometric ratios of ξ_a = 0.9, 1.3, 1.7, and 2, illustrating the higher crossover in the channel region and decreasing trend along the flow direction.

4.4 Effect of Inlet Gas Humidity

In Fig. 10a, higher anode humidity levels result in a significant increase in output voltage under high loads. At 30 s, the voltage values are 0.448, 0.488, 0.522, and 0.563 V at humidity levels of 20%, 30%, 50%, and 80%, respectively (Fig. 10b). The magnitude of voltage undershoot decreases accordingly, with values of 0.142, 0.073, 0.023, and −0.02 V, respectively.

These changes can be attributed to a reduction in ohmic polarization loss due to membrane hydration.

Fig. 10c summarizes the dynamic response of dissolved H_2 within the PEM, showing a significant decrease with increasing anode humidity, regardless of the load condition. At 30 s, the dissolved H_2 concentration is 0.703, 0.678, 0.629, and 0.556 mol m^{-3} for anode humidities of 20%, 30%, 50%, and 80%, respectively (Fig. 10d).

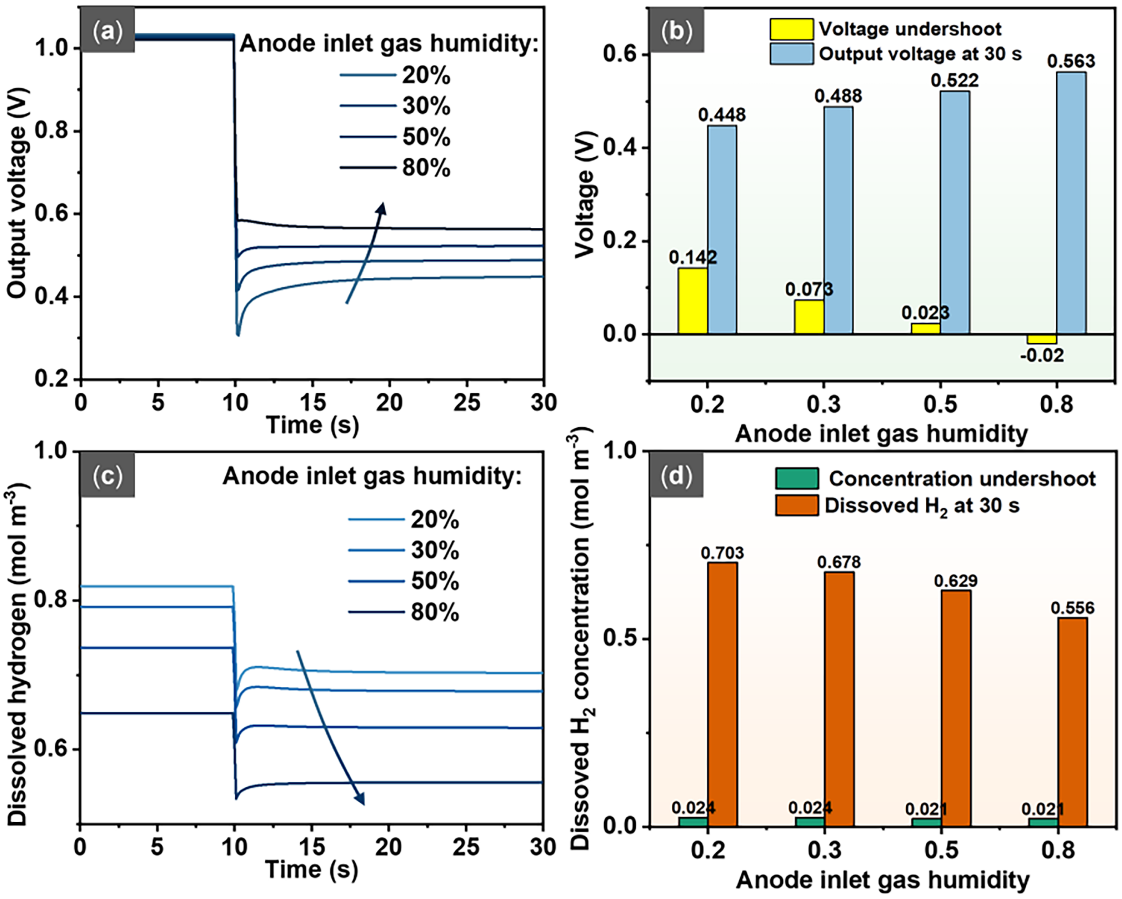

Figure 10: Effect of anode inlet humidity (20%, 30%, 50%, 80% RH) on fuel cell performance under a step load from 10 to 1800 mA cm^{-2} within 0.2 s (from 9.9 s to 10.1 s) at 90°C, 130/120 kPa for the 15 μm PEM: (**a**) Dynamic response of output voltage (increasing from 0.448 to 0.563 V at 30 s with rising anode humidity); (**b**) Voltage undershoot and steady-state voltage at 30 s (undershoot decreasing from 0.142 to −0.02 V with rising anode humidity); (**c**) Dynamic response of dissolved H_2 concentration (decreasing from 0.703 to 0.556 mol m^{-3} at 30 s with rising anode humidity); (**d**) Dissolved H_2 undershoot and steady-state concentration at 30 s.

This decrease is a result of increased water vapor diluting the H_2 gas concentration within the aCL (refer to Fig. 11a), leading to a subsequent decrease in dissolved H_2 concentration.

Fig. 11b summarizes the dynamic responses of H_2 crossover flux, revealing a significant increase from 3.5–4.6 to 5.1–5.6 mA cm^{-2} as anode humidity rises from 20% to 80%. This increase is attributed to the enhanced gas diffusion coefficient within the PEM (Fig. 11c) due to the increased water content in the membrane. Fig. 11d compares the change rates of H_2 crossover under different anode gas humidities. The rate of decrease in H_2 crossover demonstrates a significant increase with rising humidity, while the subsequent rate of increase exhibits a slight decrease. These variations are closely associated with the dynamics of local H_2 gas concentration and membrane water content. When the load abruptly increases, the concentration of anode H_2 gas decreases significantly with rising humidity, resulting in a more rapid decline in H_2 crossover. However, the subsequent increase in membrane water content diminishes with higher humidity (Fig. S2), leading to a slower rebound in H_2 crossover at elevated humidity levels.

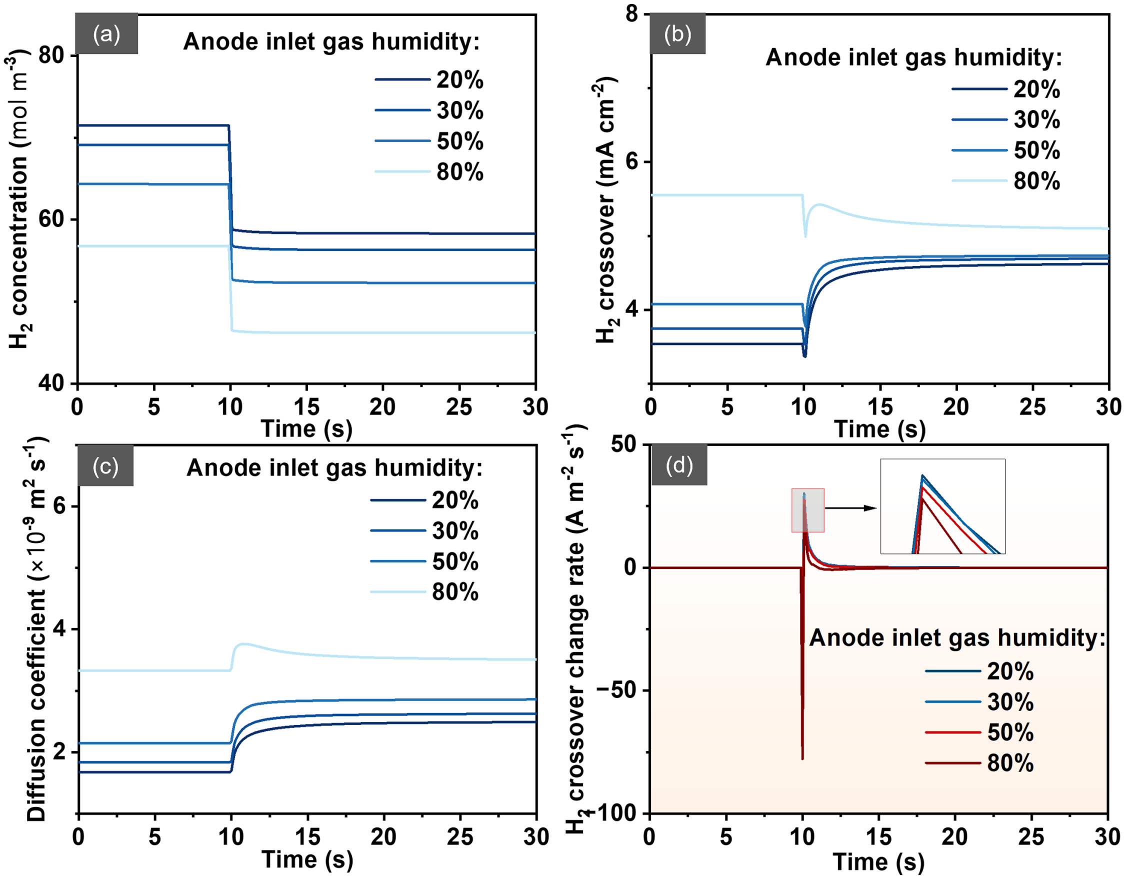

Figure 11: Mechanistic analysis of hydrogen transport under a step load from 10 to 1800 mA cm^{-2} within 0.2 s (from 9.9 to 10.1 s) at 90°C, 130/120 kPa for the 15 μm PEM with anode humidity levels (20%–80% RH), illustrating the competition between dilution and diffusion enhancement: (**a**) H_2 gas concentration in the aCL (decreasing with humidity due to dilution); (**b**) H_2 crossover flux (increasing from 3.5–4.6 to 5.1–5.6 mA cm^{-2} despite dilution); (**c**) Diffusion coefficient of dissolved H_2 (increasing with membrane hydration); (**d**) Change rates of crossover flux.

Fig. 12a–d summarizes the distributions of H_2 crossover within the PEM at 11 s. Consistent with the average dynamic response, H_2 crossover increases by approximately 0.8 mA cm^{-2} throughout the PEM as humidity increases, particularly in the region near the gas inlet under the rib. This increase in H_2 crossover with humidity is primarily attributed to the rise in membrane water content. Fig. 12e–h demonstrates a significant increase in membrane water content as anode humidity increases, especially in the area under the rib. However, in contrast to the H_2 crossover distribution, the water content near the outlet is higher due to product accumulation. This discrepancy can be explained by the more pronounced H_2 concentration gradient between the anode and cathode, which leads to more severe H_2 crossover in the inlet area.

4.5 Design Implications and Diagnostic Insights

The parametric study yields several quantitative guidelines for automotive PEMFC operation. First, membrane thickness should be optimized between 10 and 15 μm: a 5 μm membrane increases H_2 crossover fourfold (11.4–13.2 mA cm^{-2}) posing safety concerns, whereas a 20 μm membrane causes higher ohmic loss (voltage drop ~0.1 V at 1800 mA cm^{-2}). Second, under dynamic loading, an anode stoichiometric ratio of 1.3–1.7 is recommended: ξ_a = 0.9 yields the smallest crossover undershoot (0.87 mA cm^{-2}) but may compromise reactant distribution along the channel, while $\xi_a = 2.0$ gives a larger undershoot (0.96 mA cm^{-2}) and higher steady-state crossover (4.81 mA cm^{-2}); the intermediate range balances dynamic response and fuel efficiency. Inlet humidity of 50%–80% is preferred: 80% raises steady-state crossover to 5.1–5.6 mA cm^{-2} but improves voltage by 115 mV at 1800 mA cm^{-2}. For diagnostics, the predicted open-circuit voltage drop of 210 mV and local cathode temperature rise of 0.2°C can serve as non-invasive indicators of membrane integrity. Moreover, the sign change of dJ_{cross}/dt (from negative to positive) during load steps, quantified in Figs. 6c, 8d and 11d, could be used in real-time control algorithms to estimate membrane hydration state.

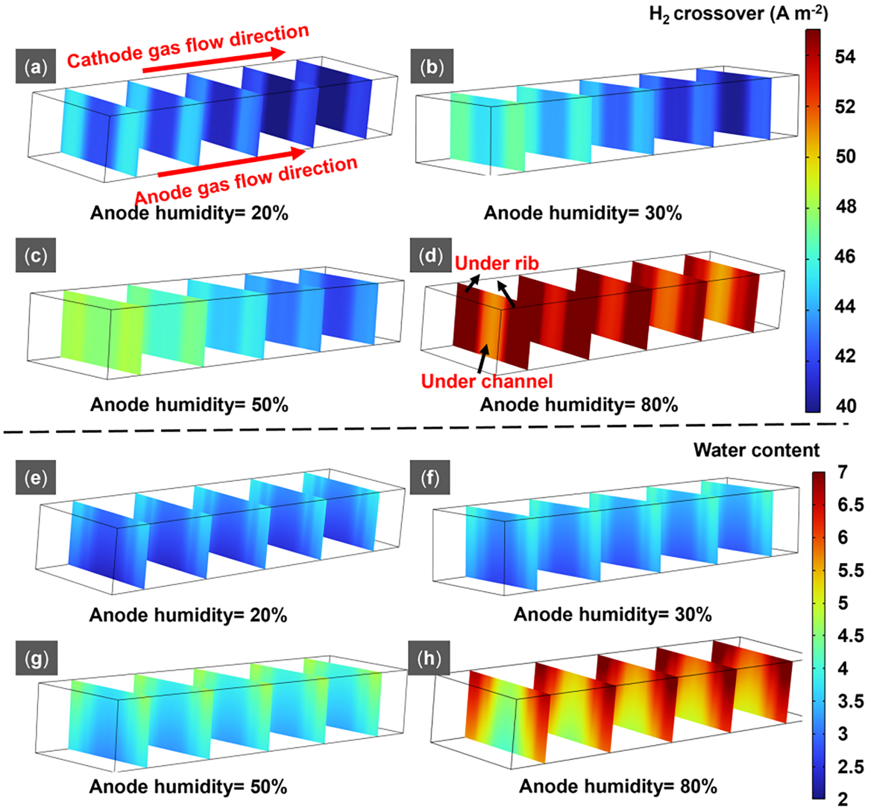

Figure 12: Spatial distributions within the 15 μm PEM at t = 11 s under step load conditions (10 → 1800 mA cm^{-2}) at 90°C, 130/120 kPa for anode humidity levels (20%, 30%, 50%, 80% RH): (**a**–**d**) H_2 crossover flux (increasing by ~0.8 mA cm^{-2}, peak values near inlet under rib); (**e**–**h**) Water content (higher near outlet due to product accumulation).

5 Conclusions

This study presents a novel three-dimensional model designed to investigate H_2 crossover phenomena in PEMFCs under dynamic loading conditions. The model incorporates essential processes including hydrogen dissolution, diffusion, convection, release, and electrochemical reactions. A particular emphasis is placed on the significant impact of H_2 crossover on both the open circuit voltage and the local thermal dynamics within the fuel cell. Using the developed model, this research systematically explores the effects of dynamic loading profiles, membrane thickness, stoichiometric ratios, and inlet humidity on H_2 crossover evolution along a single channel. The numerical simulations reveal complex interactions among these parameters and their influence on H_2 crossover dynamics. The mechanisms underlying these observations are rigorously examined. The principal findings are summarized as follows:

(1) **Spatiotemporal Variations of H_2 Crossover:** H_2 crossover within the PEM exhibits significant spatiotemporal variation influenced by the current load, membrane hydration level, and anode H_2 gas concentration. Under low current loads, the channel region experiences higher H_2 crossover levels, exceeding those in the rib region by 0.1–0.7 mA cm^{-2}, primarily due to a steeper H_2 concentration gradient. Conversely, at high current loads, H_2 crossover in the rib region increases markedly, surpassing that in the channel region by 0.1–0.4 mA cm^{-2}; this phenomenon is linked to membrane swelling resulting from enhanced hydration.

(2) **Impact of Membrane Thickness:** Reducing the PEM thickness from 20 to 5 μm results in a decrease in the overall power loss of the fuel cell but significantly increases H_2 crossover, increasing approximately fourfold, from 2.8–3.6 to 11.4–13.2 mA cm^{-2}. This heightened crossover is primarily attributed to the shorter transport path, which leads to enhanced levels of dissolved H_2 and dynamic undershoot effects. Notably, the rate of change in H_2 crossover during load variations increases as membrane thickness decreases, demonstrating an inverse relationship between diffusion and membrane thickness.

(3) **Effect of Stoichiometric Ratio:** Increasing the anode stoichiometric ratio from 0.9 to 2.0 markedly enhances the dissolved H_2 gradient at elevated current loads, resulting in an increase in H_2 crossover from approximately 2.7–4.1 to 3.5–4.3 mA cm^{-2}, particularly in the channel region. As the load rapidly increases, the H_2 crossover flux initially declines sharply, followed by a gradual rise and eventual stabilization, creating an undershoot. The initial decline is due to the reduction in anode H_2 concentration, while the subsequent rise is driven by increased membrane water content. An increased stoichiometric ratio raises the anode H_2 concentration, which slows the initial decline rate and accelerates the rate of the subsequent increase.

(4) **Influence of Anode Humidity:** Enhancing anode humidity from 20% to 80% improves overall fuel cell performance by 115 mV at 1800 mA cm^{-2} and decreases voltage undershoot by 142 mV due to membrane hydration. It also concurrently leads to a decrease in dissolved H_2 due to the dilution effect of water vapor. However, H_2 crossover flux increases from 3.5–4.6 to 5.1–5.6 mA cm^{-2}, particularly near the gas inlet under the rib, which is attributed to an improved gas permeation coefficient resulting from membrane hydration. Furthermore, the interplay between local H_2 concentration and membrane water content significantly amplifies the rate of decrease in H_2 crossover at the moment of load change.

(5) **Model Limitations:** The present model has several simplifications that should be acknowledged:

  (i) Single-channel geometry, which does not capture multi-channel or stack-level interactions;

  (ii) Validation based on global metrics (e.g., polarization curves, total crossover current) rather than spatially resolved local measurements (e.g., PCB segmented cell techniques)—direct local validation would be ideal but is beyond the current scope, a limitation not uncommon in numerical modeling studies of this nature;

  (iii) Long-term degradation evolution (e.g., chemical aging, catalyst dissolution) is not resolved in the current transient framework;

  (iv) The membrane is assumed defect-free, neglecting potential pinholes or inhomogeneities that may exist in real membranes;

  (v) Although the model is non-isothermal, the detailed effects of local heating (e.g., hot spots and their impact on mechanical stress) are not quantitatively analyzed;

  (vi) Mechanical degradation phenomena (e.g., membrane swelling, creep, compressive stress relaxation) relevant to safety and lifetime are not considered;

  (vii) Parametric sensitivity of key transport parameters (H_2 diffusion coefficient, dissolution rate, and hydraulic permeability) within ±20%–50% uncertainty bounds has not been quantified;

(viii) Characteristic time scales (τ) for gas-phase H_2 transport, membrane hydration, and thermal diffusion, and their explicit correlation with the sign change of H_2 crossover flux, have not been quantitatively decomposed.

These limitations do not undermine the main mechanistic conclusions but highlight priorities for future model extensions.

Finally, this study provides an advanced theoretical model for investigating H_2 crossover dynamics. The simulation results significantly enhance our understanding of transient hydrogen transport in PEMFCs. Future work will focus on: (i) experimental validation of the predicted local distributions and extension to multi-cell stack configurations; (ii) comprehensive parametric sensitivity analysis of transport parameters within ±20%–50% bounds; (iii) quantitative decomposition of characteristic time scales via linearized perturbation analysis; and (iv) experimental validation of H_2 crossover under non-OCV (load) conditions, thereby bridging the gap between the present modeling framework and practical fuel cell operation.

Acknowledgement: Not applicable.

Funding Statement: This project is supported by the National Natural Science Foundation of China (Grant No. 52406263) and the State Administration of Foreign Experts Affairs (China) (Grant No. Y20250131).

Author Contributions: The authors confirm contribution to the paper as follows: Wenxin Luo: Writing—original draft, Methodology, Data curation, Investigation; Kaiwen Wang: Validation, Formal analysis, Visualization, Investigation; Pugalenthiyar Thondaiman: Resources, Writing—review & editing; Qianqian Wang: Supervision, Conceptualization, Funding acquisition. All authors reviewed and approved the final version of the manuscript.

Availability of Data and Materials: The data that support the findings of this study are available from the Corresponding Author, Qianqian Wang, upon reasonable request.

Ethics Approval: Not applicable.

Conflicts of Interest: The authors declare no conflicts of interest.

Supplementary Materials: The supplementary material is available online at https://www.techscience.com/doi/10.32604/fhmt.2026.082228/s1.

References

1. Mo S, Du L, Huang Z, Chen J, Zhou Y, Wu P, et al. Recent advances on PEM fuel cells: from key materials to membrane electrode assembly. Electrochem Energy Rev. 2023;6(1):28. doi:10.1007/s41918-023-00190-w.
2. Cullen DA, Neyerlin KC, Ahluwalia RK, Mukundan R, More KL, Borup RL, et al. New roads and challenges for fuel cells in heavy-duty transportation. Nat Energy. 2021;6(5):462–74. doi:10.1038/s41560-021-00775-z.
3. Ren P, Pei P, Li Y, Wu Z, Chen D, Huang S. Degradation mechanisms of proton exchange membrane fuel cell under typical automotive operating conditions. Prog Energy Combust Sci. 2020;80:100859. doi:10.1016/j.pecs.2020.100859.
4. Lü W, Liu Z, Wang C, Mao Z, Zhang M. The effects of pinholes on proton exchange membrane fuel cell performance. Int J Energy Res. 2011;35(1):24–30. doi:10.1002/er.1728.
5. Ding F, Zou T, Wei T, Chen L, Qin X, Shao Z, et al. The pinhole effect on proton exchange membrane fuel cell (PEMFC) current density distribution and temperature distribution. Appl Energy. 2023;342:121136. doi:10.1016/j.apenergy.2023.121136.
6. Li S, Wei X, Jiang S, Yuan H, Ming P, Wang X, et al. Hydrogen crossover diagnosis for fuel cell stack: an electrochemical impedance spectroscopy based method. Appl Energy. 2022;325(7):119884. doi:10.1016/j.apenergy.2022.119884.

7. Pei P, Wu Z, Li Y, Jia X, Chen D, Huang S. Improved methods to measure hydrogen crossover current in proton exchange membrane fuel cell. Appl Energy. 2018;215:338–47. doi:10.1016/j.apenergy.2018.02.002.
8. Wallnöfer-Ogris E, Poimer F, Köll R, Macherhammer MG, Trattner A. Main degradation mechanisms of polymer electrolyte membrane fuel cell stacks—Mechanisms, influencing factors, consequences, and mitigation strategies. Int J Hydrog Energy. 2024;50:1159–82. doi:10.1016/j.ijhydene.2023.06.215.
9. Yao Z, Zhou F, Tu C, Tan J, Pan M. Decay behaviour of ultrathin reinforced membranes in PEMFCs subjected to the combination of mechanical/chemical accelerated stress testing. Int J Hydrogen Energy. 2024;50(3):200–8. doi:10.1016/j.ijhydene.2023.08.101.
10. Jung A, Oh J, Han K, Kim MS. An experimental study on the hydrogen crossover in polymer electrolyte membrane fuel cells for various current densities. Appl Energy. 2016;175(5):212–7. doi:10.1016/j.apenergy.2016.05.016.
11. Ade N, Wilhite B, Goyette H, Mannan MS. Intensifying vehicular proton exchange membrane fuel cells for safer and durable, design and operation. Int J Hydrogen Energy. 2020;45(7):5039–54. doi:10.1016/j.ijhydene.2019.12.011.
12. Chu T, Tang Q, Wang Q, Wang Y, Du H, Guo Y, et al. Experimental study on the effect of flow channel parameters on the durability of PEMFC stack and analysis of hydrogen crossover mechanism. Energy. 2023;264:126286. doi:10.1016/j.energy.2022.126286.
13. Hwang BC, Oh SH, Lee MS, Lee DH, Park KP. Decrease in hydrogen crossover through membrane of polymer electrolyte membrane fuel cells at the initial stages of an acceleration stress test. Korean J Chem Eng. 2018;35(11):2290–5. doi:10.1007/s11814-018-0142-5.
14. Zhou X, Qiu D, Peng L, Lai X. Numerical and experimental characterization of gas permeation through membranes with consideration of mechanical degradation in proton exchange membrane fuel cells. J Power Sources. 2023;556(1):232489. doi:10.1016/j.jpowsour.2022.232489.
15. Kocha SS, Yang JD, Yi JS. Characterization of gas crossover and its implications in PEM fuel cells. AlChE J. 2006;52(5):1916–25. doi:10.1002/aic.10780.
16. Tang F, Tang Z, Yang Y, Li B, Zhang C, Ming P. A general equation for the polarization curves of proton exchange membrane fuel cell under hydrogen crossover current measurement. J Electroanal Chem. 2023;937(1):117425. doi:10.1016/j.jelechem.2023.117425.
17. Schoemaker M, Misz U, Beckhaus P, Heinzel A. Evaluation of hydrogen crossover through fuel cell membranes. Fuel Cells. 2014;14(3):412–5. doi:10.1002/fuce.201300215.
18. Li S, Wei X, Dai H, Yuan H, Ming P. Voltammetric and galvanostatic methods for measuring hydrogen crossover in fuel cell. iScience. 2022;25(1):103576. doi:10.1016/j.isci.2021.103576.
19. Hu Z, Xu L, Huang Y, Li J, Ouyang M, Du X, et al. Comprehensive analysis of galvanostatic charge method for fuel cell degradation diagnosis. Appl Energy. 2018;212(4):1321–32. doi:10.1016/j.apenergy.2018.01.005.
20. Shan J, Gazdzicki P, Lin R, Schulze M, Friedrich KA. Local resolved investigation of hydrogen crossover in polymer electrolyte fuel cell. Energy. 2017;128(45):357–65. doi:10.1016/j.energy.2017.03.104.
21. Baik KD, Kong IM, Hong BK, Kim SH, Kim MS. Local measurements of hydrogen crossover rate in polymer electrolyte membrane fuel cells. Appl Energy. 2013;101:560–6. doi:10.1016/j.apenergy.2012.06.034.
22. Weber AZ. Gas-crossover and membrane-pinhole effects in polymer-electrolyte fuel cells. J Electrochem Soc. 2008;155(6):B521–31. doi:10.1149/1.2898130.
23. Vilekar SA, Datta R. The effect of hydrogen crossover on open-circuit voltage in polymer electrolyte membrane fuel cells. J Power Sources. 2010;195(8):2241–7. doi:10.1016/j.jpowsour.2009.10.023.
24. Kusoglu A, Weber AZ. A mechanistic model for pinhole growth in fuel-cell membranes during cyclic loads. J Electrochem Soc. 2014;161(8):E3311–22. doi:10.1149/2.036408jes.
25. Giner-Sanz JJ, Ortega EM, Pérez-Herranz V. Hydrogen crossover and internal short-circuit currents experimental characterization and modelling in a proton exchange membrane fuel cell. Int J Hydrogen Energy. 2014;39(25):13206–16. doi:10.1016/j.ijhydene.2014.06.157.
26. Omrani R, Shabani B. An analytical model for hydrogen and nitrogen crossover rates in proton exchange membrane fuel cells. Int J Hydrogen Energy. 2020;45(55):31041–55. doi:10.1016/j.ijhydene.2020.08.089.
27. Ji C, Niu H, Wang S, Liang C, Li X, Yang J. Research on two-phase flow considering hydrogen crossover in the membrane for a polymer electrolyte membrane fuel cell. Int J Energy Res. 2019;43(7):2881–96. doi:10.1002/er.4430.

28. Nguyen TT, Fushinobu K. Effect of operating conditions and geometric structure on the gas crossover in PEM fuel cell. Sustain Energy Technol Assess. 2020;37:100584. doi:10.1016/j.seta.2019.100584.
29. Li Y, Zhou Z, Liu X, Wu WT. Modeling of PEM fuel cell with thin MEA under low humidity operating condition. Appl Energy. 2019;242:1513–27. doi:10.1016/j.apenergy.2019.03.189.
30. Mohamed HFM, Ito K, Kobayashi Y, Takimoto N, Takeoka Y, Ohira A. Free volume and permeabilities of O_2 and H_2 in Nafion membranes for polymer electrolyte fuel cells. Polymer. 2008;49(13–14):3091–7. doi:10.1016/j.polymer.2008.05.003.
31. Kusoglu A, Weber AZ. New insights into perfluorinated sulfonic-acid ionomers. Chem Rev. 2017;117(3):987–1104. doi:10.1021/acs.chemrev.6b00159.
32. Singh R, Sui PC, Wong KH, Kjeang E, Knights S, Djilali N. Modeling the effect of chemical membrane degradation on PEMFC performance. J Electrochem Soc. 2018;165(6):F3328–36. doi:10.1149/2.0351806jes.
33. Trinke P, Haug P, Brauns J, Bensmann B, Hanke-Rauschenbach R, Turek T. Hydrogen crossover in PEM and alkaline water electrolysis: mechanisms, direct comparison and mitigation strategies. J Electrochem Soc. 2018;165(7):F502–13. doi:10.1149/2.0541807jes.
34. Zhang H, Li J, Tang H, Lin Y, Pan M. Hydrogen crossover through perfluorosulfonic acid membranes with variable side chains and its influence in fuel cell lifetime. Int J Hydrogen Energy. 2014;39(28):15989–95. doi:10.1016/j.ijhydene.2014.01.076.
35. Ding F, Zhan X, Wei T, Sun J, Huang H, Cui Y, et al. Similarities and differences between internal short-circuit current and hydrogen crossover current in a proton exchange membrane fuel cell. Chem Eng J. 2024;494(7867):153091. doi:10.1016/j.cej.2024.153091.
36. Zhang J, Zhang H, Wu J, Zhang J. Fuel cell open circuit voltage. In: Pem fuel cell testing and diagnosis. Amsterdam, The Netherlands: Elsevier; 2013. p. 187–200.
37. Zhang J, Zhang H, Wu J, Zhang J. Hydrogen crossover. In: Pem fuel cell testing and diagnosis. Amsterdam, The Netherlands: Elsevier; 2013. p. 171–85.
38. Ngo PM, Karimata T, Saitou T, Ito K. Effect of current density on membrane degradation under the combined chemical and mechanical stress test in the PEMFCs. J Power Sources. 2023;556(25):232446. doi:10.1016/j.jpowsour.2022.232446.
39. Wang Q, Tang F, Li B, Dai H, Zheng JP, Zhang C, et al. Investigation of the thermal responses under gas channel and land inside proton exchange membrane fuel cell with assembly pressure. Appl Energy. 2022;308(3):118377. doi:10.1016/j.apenergy.2021.118377.
40. Wang Q, Tang F, Li X, Zheng JP, Hao L, Cui G, et al. Revealing the dynamic temperature of the cathode catalyst layer inside proton exchange membrane fuel cell by experimental measurements and numerical analysis. Chem Eng J. 2023;463:142286. doi:10.1016/j.cej.2023.142286.
41. Wang Q, Tang F, Li B, Dai H, Zheng JP, Zhang C, et al. Numerical analysis of static and dynamic heat transfer behaviors inside proton exchange membrane fuel cell. J Power Sources. 2021;488(56):229419. doi:10.1016/j.jpowsour.2020.229419.
42. Trinke P, Bensmann B, Reichstein S, Hanke-Rauschenbach R, Sundmacher K. Hydrogen permeation in PEM electrolyzer cells operated at asymmetric pressure conditions. J Electrochem Soc. 2016;163(11):F3164–70. doi:10.1149/2.0221611jes.
43. Franz T, Papakonstantinou G, Sundmacher K. Transient hydrogen crossover in dynamically operated PEM water electrolysis cells—a model-based analysis. J Power Sources. 2023;559:232582. doi:10.1016/j.jpowsour.2022.232582.
44. Kang Z, Pak M, Bender G. Introducing a novel technique for measuring hydrogen crossover in membrane-based electrochemical cells. Int J Hydrogen Energy. 2021;46(29):15161–7. doi:10.1016/j.ijhydene.2021.02.054.
45. Bernt M, Schröter J, Möckl M, Gasteiger HA. Analysis of gas permeation phenomena in a PEM water electrolyzer operated at high pressure and high current density. J Electrochem Soc. 2020;167(12):124502. doi:10.1149/1945-7111/abaa68.
46. Trinke P, Keeley GP, Carmo M, Bensmann B, Hanke-Rauschenbach R. Elucidating the effect of mass transport resistances on hydrogen crossover and cell performance in PEM water electrolyzers by varying the cathode ionomer content. J Electrochem Soc. 2019;166(8):F465–71. doi:10.1149/2.0171908jes.

47. Wang Q, Tang F, Li B, Dai H, Zheng JP, Zhang C, et al. Study on the thermal transient of cathode catalyst layer in proton exchange membrane fuel cell under dynamic loading with a two-dimensional model. Chem Eng J. 2022;433(5):133667. doi:10.1016/j.cej.2021.133667.
48. Yuan H, Dai H, Ming P, Li S, Wei X. A new insight into the effects of agglomerate parameters on internal dynamics of proton exchange membrane fuel cell by an advanced impedance dimension model. Energy. 2022;253(12):124202. doi:10.1016/j.energy.2022.124202.
49. Goshtasbi A, García-Salaberri P, Chen J, Talukdar K, Sanchez DG, Ersal T. Through-the-membrane transient phenomena in PEM fuel cells: a modeling study. J Electrochem Soc. 2019;166(7):F3154–79. doi:10.1149/2.0181907jes.
50. Zang L, Hao L, Zhu X. Effect of gas crossover on the cold start process of proton exchange membrane fuel cells. Fuel. 2024;363(3):130921. doi:10.1016/j.fuel.2024.130921.
51. Baik KD, Hong BK, Kim MS. Effects of operating parameters on hydrogen crossover rate through Nafion® membranes in polymer electrolyte membrane fuel cells. Renew Energy. 2013;57(9):234–9. doi:10.1016/j.renene.2013.01.046.
52. Sakai T, Takenaka H, Wakabayashi N, Kawami Y, Torikai E. Gas permeation properties of solid polymer electrolyte (SPE) membranes. J Electrochem Soc. 1985;132(6):1328–32. doi:10.1149/1.2114111.
53. Schalenbach M, Hoefner T, Paciok P, Carmo M, Lueke W, Stolten D. Gas permeation through nafion. Part 1: measurements. J Phys Chem C. 2015;119(45):25145–55. doi:10.1021/acs.jpcc.5b04155.